

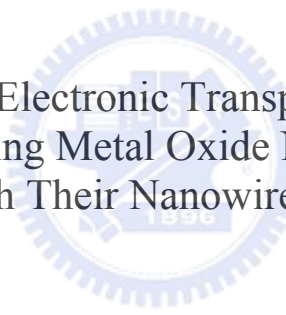
# 國立交通大學

物理研究所

博士論文

氧化物金屬奈米線及其奈米線接點之電子傳輸特性

Electronic Transport  
in Conducting Metal Oxide Nanowires and  
through Their Nanowire Contacts



研究生：林永翰

指導教授：林志忠 教授

中華民國九十六年七月

氧化物金屬奈米線及其奈米線接點之電子傳輸特性  
Electronic Transport  
in Conducting Metal Oxide Nanowires and  
through Their Nanowire Contacts

研究生：林永翰

Student：Yong-Han Lin

指導教授：林志忠 教授

Advisor：Prof. Juhn-Jong Lin

國立交通大學  
物理研究所  
博士論文



A Thesis  
Submitted to Institute of Physics  
College of Science  
National Chiao Tung University  
in Partial Fulfillment of the Requirements  
for the Degree of  
Doctor of Philosophy  
in  
Physics

July 2007

Hsinchu, Taiwan, Republic of China

中華民國九十六年七月

# 氧化物金屬奈米線及其奈米線接點之電子傳輸特性

學生：林永翰

指導教授：林志忠 教授

國立交通大學物理研究所博士班

## 摘 要

毫無疑問，瞭解電子在奈米線內部的運動行為是應用奈米線製作新穎奈米電子元件一個相當重要的步驟，然而，要能實際達成應用的目的，僅止於這樣的瞭解卻是不夠的。我們知道，任何奈米線，不論是作為元件本身或是作為傳遞訊號的導線，它都必須與外界有所接觸，這個接觸可能是元件與元件之間的連結，也可能是元件與巨觀世界之間的連結。由於相關奈米製程的步驟繁複，一個非理想的接點顯然十分容易因為污染或製程條件的些微差異而形成，而這樣一個非理想的接點極可能會改變電子的運動方式，並進而影響元件的正常操作模式。因此，徹底掌握電子在奈米線內部與在奈米線接點附近的傳輸特性是兩個同等重要的研究課題。

本篇論文即是針對上述的主題，以  $\text{RuO}_2$  與  $\text{IrO}_2$  兩種極具應用價值的氧化物金屬奈米線為主體，進行一完整的研究。 $\text{RuO}_2$  與  $\text{IrO}_2$  是具有相同結構、高度化學與熱穩定性，以及擁有相當於一般金屬導電率的過渡金屬氧化物。利用標準的電子束微影製程，以及運用不同數目的量測電極，我們不僅釐清了它們本身從室溫到液態氦溫度的電子傳輸特性，也成功地描述了電子在奈米線接點附近從室溫到液態氦溫度的運動行為。

關於  $\text{RuO}_2$  與  $\text{IrO}_2$  奈米線本身的電子傳輸特性，我們發現，與它們的單晶塊材相同，其奈米線的電阻率從室溫到液態氦溫度的變化仍舊可以用 Boltzmann 傳輸理論來成功描述。然而，對於  $\text{RuO}_2$  奈米線而言，我們發現，從理論擬合得到的 Debye 溫度卻會隨著奈米線直徑

縮小而大幅度的變小。對於直徑約 40 奈米的 RuO<sub>2</sub> 奈米線而言，其內的 Debye 溫度已變小至只有其單晶塊材 Debye 溫度的大約一半大小。對於我們所觀察到的結果，我們提出並探討了一些可能引發這種現象的物理機制，我們歸納後認為，這樣的現象應該是來自於晶格點與晶格點之間的等效鍵結力(亦即晶體的楊格彈性係數)隨著奈米線直徑變小而減弱所導致。另外，在此篇論文裡，我們將僅報告較大直徑 IrO<sub>2</sub> 奈米線的測量結果，對於較小直徑 IrO<sub>2</sub> 奈米線的進一步測量則正在進行當中。

對於電子通過 RuO<sub>2</sub> 與 IrO<sub>2</sub> 奈米線接點的傳輸行為，我們發現，對於具有較高接觸電阻的接點而言，不同材質的奈米線，其接觸電阻隨溫度變化的行為分別可以用不同的物理模型(函數關係)來成功解釋。在 RuO<sub>2</sub> 奈米線方面，我們發現，其較高阻值的接觸電阻隨溫度的變化行為可以用 thermally fluctuation-induced tunneling 的物理模型來解釋，這主要是由於在接點附近形成一個等效的絕緣層，導致電子通過接點時是以 tunneling 的方式來傳遞。在 IrO<sub>2</sub> 奈米線方面，我們發現，在溫度約 100 K 以下，其較高阻值的接觸電阻與溫度的相依關係則是遵從了  $\log R$  正比於  $T^{-1/2}$  的關係式，這主要是因為在接點附近形成了一個由顆粒狀金屬所組成的區域，使得電子通過接點時是以 hopping 的方式來傳輸。我們認為，不同材質奈米線的接觸電阻具有不同的溫度相依關係，極可能只是一個隨機的結果，亦即，接點結構乃是從兩種可能的結構當中(絕緣層或顆粒層)隨機形成，然而，這樣的結構差異也很可能是肇因於金屬電極材料(本篇論文使用 Cr/Au 作為電極材料)在不同材質的奈米線上具有不同的表面應力。更進一步的釐清我們則正在進行當中。

# 誌 謝

感謝我的父母

以及

所有曾經幫助過我的老師、學長、同學、學弟、學妹!



# Abstract

Fair understanding of the intrinsic electronic transport properties of individual nanowires (NWs) is certainly the key step for numerous nanoelectronic applications. Quantitative knowledge about the relevant electronic contacts is also very crucial in correctly interpreting the experimental results. In this work, we have studied the intrinsic electronic transport properties of individual single-crystalline RuO<sub>2</sub> and IrO<sub>2</sub> NWs, which belong to the family of transition metal oxides that have advantages of being chemically stable while possessing comparatively high conductivities. With the help of the standard electron-beam lithographic technique, individual NWs are contacted by submicron metal electrodes from above. By applying different probe configurations to our measurements, not only the intrinsic electronic transport properties of the individual as-grown NWs but also the temperature behaviours of high-resistance electronic contacts,  $R_c(T)$ , have been determined down to liquid-helium temperatures.

Two main results have been obtained. First, the measured temperature dependent resistivity of the NWs is found to agree well with the current theoretical understanding of these materials. Although they can be well described by the existing theory, we found that the Debye temperature in RuO<sub>2</sub> NWs is significantly reduced to only one half of its bulk value when the diameter of the NW decreases down to  $\approx 40$  nm. (Comparable experiments on IrO<sub>2</sub> NWs with diameters down to this scale have not been performed.) Possible mechanisms accounting for this observation have been discussed. It is conjectured that the chemical binding in the NWs may be gradually weakened as the diameter decreases.

Second, for high-resistance electronic contacts, the measured  $R_c(T)$  reveals semiconducting or insulating behaviour, i.e., it increases rapidly with decreasing temperature. However, different temperature dependence has been found

for different kind of NW. For RuO<sub>2</sub> NWs, the temperature behavior of  $R_c$  can be satisfactorily explained in terms of the thermally fluctuation-induced tunneling through a junction formed at the interface between the electrode and the NW. On the other hand, for IrO<sub>2</sub> NWs, a power law of the form  $\log R_c \propto T^{-1/2}$  over a very wide temperature range from  $\approx 100$  K down to liquid-helium temperatures has been observed. This later conduction process is ascribed to the hopping of electrons through nanoscale metal (Cr) granules incidentally formed at the contact region during the thermal evaporation of the submicron Cr/Au electrodes. Although such a difference may arise from the different surface conditions of different kinds of NWs (such as different surface stresses), we believe that either mechanism could occur even for the same kind of NW; they just appear randomly. Unfortunately, direct evidences supporting this viewpoint are not obtained in this work.



# Contents

<b>Abstract</b> . . . . .	<b>ii</b>
<b>List of Tables</b> . . . . .	<b>vi</b>
<b>List of Figures</b> . . . . .	<b>vii</b>
<b>1 Introduction</b> . . . . .	<b>1</b>
<b>2 Experimental method</b> . . . . .	<b>5</b>
2.1 Fabrication of nanowires . . . . .	5
2.1.1 RuO <sub>2</sub> . . . . .	5
2.1.2 IrO <sub>2</sub> . . . . .	8
2.2 Electrical measurements . . . . .	10
<b>3 Electronic transport in metal nanowires</b> . . . . .	<b>16</b>
3.1 Introduction . . . . .	16
3.2 Theoretical background . . . . .	16
3.3 RuO <sub>2</sub> . . . . .	20
3.3.1 Nanowires with diameters $\gtrsim 100$ nm . . . . .	24
3.3.2 Nanowires with diameters $< 100$ nm . . . . .	37
3.3.2.1 Size-dependent Debye temperature . . . . .	37
3.4 IrO <sub>2</sub> . . . . .	46
<b>4 Electronic transport through metal nanowire contacts</b> . . . . .	<b>51</b>
4.1 Introduction . . . . .	51
4.2 RuO <sub>2</sub> . . . . .	54
4.2.1 Fluctuation-induced tunneling conduction . . . . .	54
4.3 IrO <sub>2</sub> . . . . .	60



4.3.1 Electron hopping conduction . . . . .	60
<b>5 Conclusion . . . . .</b>	<b>68</b>
<b>References . . . . .</b>	<b>70</b>



## List of Tables

Table 3.1	Sample parameters for the eight RuO <sub>2</sub> NWs measured by the 4-p method. Because the NWs have square cross sections, the diameter here means the side length of the square. The large uncertainties in length (defined as the length of the section that we actually probe) are mainly due to the large widths of the voltage probes and thus result in the large uncertainties in resistivity. . . . .	22
Table 3.2	Values of the relevant parameters for the eight RuO <sub>2</sub> NWs measured by the 4-p method. . . . .	28
Table 3.3	Values of the relevant parameters for the two IrO <sub>2</sub> NWs measured by the 4-p method. For both samples, $W \approx 180 \pm 5$ nm and $L \approx 0.83 \pm 0.01 \mu\text{m}$ . The uncertainties in resistivities mainly arise from the uncertainties in the dimensions of the NWs. . . . .	49
Table 4.1	Values of relevant parameters for four high-resistance NW devices, as determined from the 2-probe method. For each device, the NW resistance $R_s(300 \text{ K})$ was estimated from the 4-probe method, while the junction area $A$ was determined from the SEM image. . . . .	59
Table 4.2	Values of the relevant parameters for the three-probe and two-probe electrical measurement configurations implemented on the Ir-3 NW contacted by three submicron Cr/Au (10/90 nm) electrodes. The Ir-3 NW has a hypotenuse $W \approx 115 \pm 5$ nm, length $L \approx 0.7 \mu\text{m}$ , and the sample resistance $R_s(300 \text{ K}) \approx 0.5 \text{ k}\Omega$ . $R_\infty$ and $T_0$ are defined in Eq. (4.4). . . . .	63

## List of Figures

Figure 2.1 Rutile structure. . . . .	6
Figure 2.2 TEM image for a RuO <sub>2</sub> NW. . . . .	7
Figure 2.3 (a) Tilted FESEM image of as-grown IrO <sub>2</sub> NWs revealing nearly triangular cross sections. (b) Schematic plot of the geometry for a NW. (c) XRD pattern of the NWs. . . . .	9
Figure 2.4 Schematic plot of making electrical contacts onto individual NWs. . . . .	12
Figure 2.5 (a) Schematic diagram for a single NW (thick bar) with four electronic contacts on it and the equivalent circuit model. $R_s$ denotes the resistance of each segment of the NW (i.e., the sample resistance). $R_{c1}$ , $R_{c2}$ , $R_{c3}$ and $R_{c4}$ denote the electronic contact resistances between the NW and the sub-micron electrodes 1, 2, 3 and 4, respectively. $R_{el,i}$ denotes the submicron-electrode resistance of the $i$ th electrode. Four-probe (b), three-probe (c) and two-probe (d) measurement configurations, and the corresponding measured resistances. In (d), the approximations $R_{c2} \approx R_{c3} \equiv R_c$ and $R_{el,2} \approx R_{el,3} \equiv R_{el}$ are assumed (see text). . . . .	13
Figure 2.6 Additional probe configurations needed to extract the resistance of each electronic contact. . . . .	15
Figure 3.1 Typical temperature behaviour of RuO <sub>2</sub> NWs. . . . .	21
Figure 3.2 SEM image of the Ru-8 NW. . . . .	23
Figure 3.3 Variation of the resistivity at $T = 300$ K with diameter of the NW for the NWs measured in the present work. . . . .	25
Figure 3.4 log-log plot of the variation of the measured normalized resistivity, $(\rho - \rho_0)/\rho_0$ , as a function of temperature for two NWs with diameters $\approx 100$ nm. . . . .	26
Figure 3.5 Variation of $\Theta_D$ with diameter. . . . .	29
Figure 3.6 Variation of $\Theta_E$ with diameter. . . . .	30
Figure 3.7 Variation of $\beta_{BG}/\rho_0$ with diameter. . . . .	31

Figure 3.8	Variation of $\rho_0$ with diameter. . . . .	32
Figure 3.9	Best fit for the sample Ru-4 by intentionally setting $\Theta_D$ and $\Theta_E$ to their bulk values (i.e., 400 and 790 K, respectively) and leaving only $\rho_0$ and $\beta_{BG}$ as free variables. . . . .	33
Figure 3.10	Best fit for the sample Ru-4 to the Eq. (3.10) by intentionally setting $\Theta_D$ and $\Theta_E$ to their bulk values (i.e., 400 and 790 K, respectively) and leaving only $\rho_0$ , $\beta_{BG}$ , and $\beta_{int}$ as free variables. . . . .	36
Figure 3.11	Variation of $\beta_{int}$ with diameter. . . . .	38
Figure 3.12	$f(x)$ as a function of $x$ for a material with a $\Theta_D$ at several different temperatures. . . . .	43
Figure 3.13	Resistivity as a function of temperature for two IrO <sub>2</sub> NWs measured by the four-probe method. The symbols are the experimental data and the solid lines are the theoretical predictions of equation (3.11). The inset shows the SEM image of one NW contacted by four Cr/Au electrodes. . . . .	47
Figure 3.14	Log-log plot of the variation of the normalized resistivity $\Delta\rho/\rho_0 = (\rho - \rho_0)/\rho_0$ with temperature for the two IrO <sub>2</sub> NWs studied in figure 3.13. Notice that the scales of the axes are different in (a) and (b). The contribution from the $\rho_{int}/\rho_0$ term in the Ir-1 NW has the same magnitude as that ( $\sim 10^{-3}$ ) in the Ir-2 NW, and thus is outside the range displayed in (a). . . . .	50
Figure 4.1	Three typical temperature behaviours of the measured resistance $R$ , as determined from the 2-p method. . . . .	53
Figure 4.2	Resistance as a function of temperature for two high-resistance contacts in series, as determined from the 2-probe method on the NW device C3 (see Table 4.1). The inset shows a plot of $\log R$ versus $T^{-1}$ for the same NW device. The straight solid line indicates the thermal activation conduction. . . . .	55
Figure 4.3	Double logarithmic plot of the resistances versus temperature for four high-resistance NW devices, as determined from the 2-probe method. The symbols are the experimental data and the solid curves are the theoretical fits to Eq. (4.1). . . . .	58

Figure 4.4 (a) Resistances as a function of temperature for the 2-probe and 3-probe measurement configurations as depicted in Figs. 2.5(c) and (d). The inset shows  $\log R$  as a function of  $1/T$ . (b)  $\log R$  as a function of  $T^{-1/2}$ . Since  $R_{2-p} \approx R_{c2} + R_{c3}$  and  $R_{3-p} \approx R_{c3}$ , the difference between the two curves is simply the electronic contact resistance  $R_{c2}$ . . . . . 62

Figure 4.5 (a) AFM image of a thin Cr layer with a mean thickness of 10 nm prepared by thermal-evaporation deposition on a mica substrate. (b) Surface profile along the line indicated in (a), showing a distribution of disk-shaped grains having radius of  $\sim$  several tens nm and height of  $\approx 2-6$  nm. . . . . 65



# Chapter 1

## Introduction

Over the past decade, nanostructures have received much attention because they not only have great potential for novel industrial applications but also could provide a peculiar system for fundamental researches on issues about dimensionality and space-confined phenomena. Among the various nanostructures, self-assembled quasi-one-dimensional (Q1D) metallic nanowires (NWs) are of particular interest due to their promising applicability in the future nanoelectronics as elemental devices or as probes that diagnose functional circuitry. For instance, the molecular carbon nanotubes (CNTs) are shown to behave (in some cases) ballistically and be capable of sustaining extremely high current densities [1]. Prototypical nanoelectronic devices based on a single CNT have been proposed and tested [2]. To date, in addition to the extensively studied CNTs [1, 2], great amounts of efforts have been focusing on quasi-one-dimensional semiconductors [3] and their binary compounds including Si [4], ZnO [5], GaN [6], etc.

Of course, for all fascinating applications to be true, fair understanding of the intrinsic electronic transport properties of these Q1D metallic NWs is the very first and key step for the realization of numerous possibilities. However, although nowadays various metallic NW systems have been successfully synthesized, electrical characterizations on individual metallic NWs have been comparatively less reported with only very few exceptions like metallic silicide [7] and semi-metallic Bi [8, 9]. This lack of reports mainly originates from the problem of uncontrollable surface oxidation that largely hinders reliable electrical measurements from being taken [8]. Measurements so far were thus mostly performed simultaneously on a great number of NWs imbedded in an insulating porous template, by using the simple 2-probe method. In that way, the influences of the contacts apparently cannot be explicitly excluded and the

unique properties of individual NWs could also be easily smeared out.

In this context, conducting metal oxides, such as RuO<sub>2</sub> and IrO<sub>2</sub>, that have advantages of being chemically stable while possessing comparatively high conductivities, can thus provide an alternative and excellent choice for nanodevice-related applications and most of all, fundamental electronic transport studies, from which the information inferred over a wide range of temperature (and, further, with the application of magnetic fields) will help clarify the electronic conduction mechanism in metal and semiconductor NWs.

Recently, syntheses of single-crystalline RuO<sub>2</sub> and IrO<sub>2</sub> NWs have been reported by means of different techniques including cryogenic decomposition [10], metal-organic chemical vapor deposition [11], reactive sputtering [12], and many others [13, 14, 15]. Nevertheless, despite the fact that they are metallic oxides with superior chemical stabilities, the intrinsic temperature dependent electronic transport properties of these highly applicable materials down to the nanoscale have not yet been fully characterized so far.

This fact may result from another frequently encountered technical difficulty. Since exploring the electronic transport properties in these Q1D systems requires the connections of the instruments to the individual nanostructures, nanofabrication techniques such as the electron-beam lithography (EBL) and the focused ion beam deposition are usually employed to accomplish this need. However, it is known that fabrication of reliable electronic contacts to the nanodevices has been a nontrivial issue, because very often an imperfect contact inevitably forms and may possess a non-negligible temperature dependent contact resistance,  $R_c(T)$ , which in turn is prone to complicate the experiments and could seriously mislead the physical interpretation of the data. The high-resistance  $R_c$  may be as a result of the surface contamination of the NW, or the minor break of the electrode at the contact where it just touches the NW. Either could be easily introduced due to the complexity of the whole fabrication process.

From the physical point of view, in the cases involving semiconductors, the contact between a metal electrode and a semiconductor NW usually forms a Schottky barrier, whose properties have been extensively studied [16]. A

different situation concerning heavily doped semiconductor NW has also been discussed [17]. On the contrary, the electrical properties of the contact between a metal electrode and a metal NW have not yet been much addressed in the literature. In the case of metal NWs, since the NWs may readily be separated from the electrode by a layer of some insulator (oxidation, contamination, an amorphous coating, or a break, etc.) of a few nm thick, the underlying physics of how electron waves transmit through such a nanoscale interface should be of fundamental interest and urgent industrial concerns.

In this work, we report the electronic transport measurements on individual single-crystalline RuO<sub>2</sub> and IrO<sub>2</sub> NWs fabricated by the thermal evaporation method and the metal-organic chemical vapor deposition method, respectively. With the help of the EBL technique, individual NWs were contacted by submicron electrodes from above. Utilizing different probe configurations in our measurements, not only the intrinsic electronic transport properties of individual NWs but also the temperature dependent high-resistance electronic contacts (which incidentally formed at the interfaces between the lithographic-patterned submicron electrodes and the NWs) have been determined from 300 K down to liquid-helium temperatures.

We found that the electronic transport properties of our as-grown NWs can be explained in terms of the current theoretical understanding for these materials. The measured temperature dependent resistivities are well accounted for by the scattering of electrons with phonons. However, for RuO<sub>2</sub> NWs with diameters of several tens nm, the effective Debye temperature was found to be largely reduced as compared with its bulk value.<sup>1</sup> It is conjectured that the chemical binding of the lattice may be weakened as the diameter of the NW decreases.

On the other hand, instead of providing a solution to the problem resulting in the high-resistance  $R_c$ , we demonstrated that the temperature behavior of  $R_c$ , however, can be well understood in terms of two existing phenomenological

---

<sup>1</sup>Investigations of the IrO<sub>2</sub> NWs with diameters down to the similar scales have not been performed yet because of the experimental difficulty of patterning four submicron electrodes onto such NWs, of which the lengths are rather shorter than those of the RuO<sub>2</sub> NWs.



theories, one for RuO<sub>2</sub> NWs, and one for IrO<sub>2</sub> NWs. Although such a difference may arise from the different surface conditions of different kinds of NWs (such as different surface stresses), we believe that either mechanism could occur even for the same kind of NWs; they just appear randomly. Unfortunately, direct evidences supporting this viewpoint are not obtained in this work.

To our knowledge, the present work is the first quantitative electrical characterization on these highly applicable materials down to the nanoscale, and also over such a wide range of temperature.



# Chapter 2

## Experimental method

### 2.1 Fabrication of nanowires

The NWs used in the present work are provided by Profs. Fu-Rong Chen and Ji-Jung Kai's group at the Department of Engineering and System Science of National Tsing Hua University ( $\text{RuO}_2$ ) and by Prof. Ying-Sheng Huang's group at the Department of Electronic Engineering of National Taiwan University of Science and Technology ( $\text{IrO}_2$ ). The fabrication processes are briefly given here. Detailed descriptions of fabrication processes and other material characterizations for each kind of NWs can be found in the references as indicated in the text.

#### 2.1.1 $\text{RuO}_2$

Ruthenium dioxide,  $\text{RuO}_2$ , together with several other oxides, such as  $\text{IrO}_2$  and  $\text{OsO}_2$ , crystallizes in the rutile structure (Fig. 2.1) and belongs to the family of transition metal oxides that exhibit metallic conductivities comparable with those of the parent metals themselves [18, 19]. Owing to its excellent thermal and chemical stability [20, 21], it has been investigated for applications in many diverse fields. For example, it has been used as resistive thermometers in cryogenics [22], as corrosion-resistant low-overpotential electrodes for chlorine and oxygen evolution in electrolysis [23], and as electrochemical capacitors for energy storage in power industry [24]. Moreover, in addition to being a strip-line conductor [25] and an electrical contact material [26] in vast electronics,  $\text{RuO}_2$  as well finds its application in modern very large scale integrated circuits as an outstanding diffusion barrier between Al and Si in contact metallizations [27].

Single-crystalline  $\text{RuO}_2$  NWs were self-assembled by applying the thermal

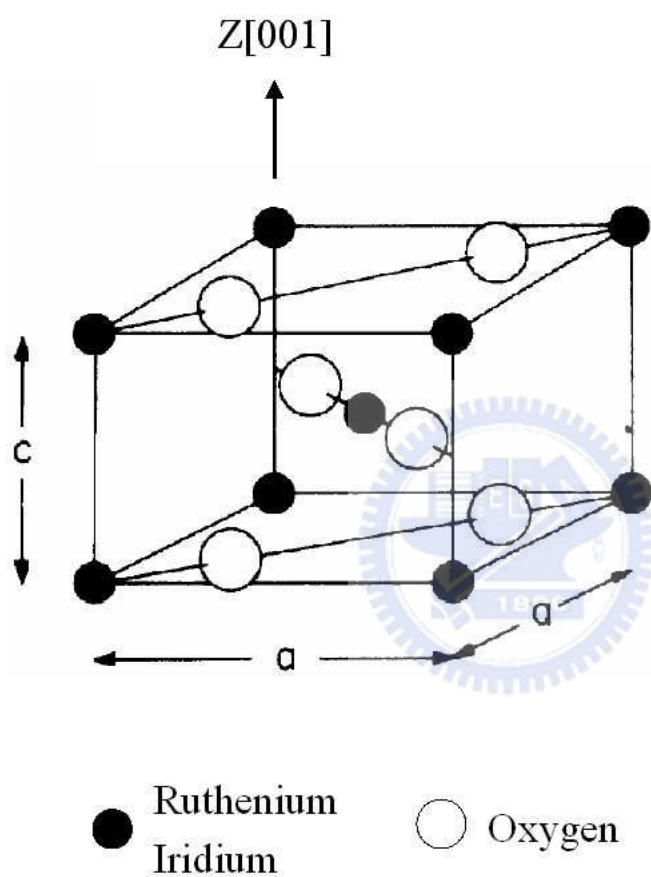
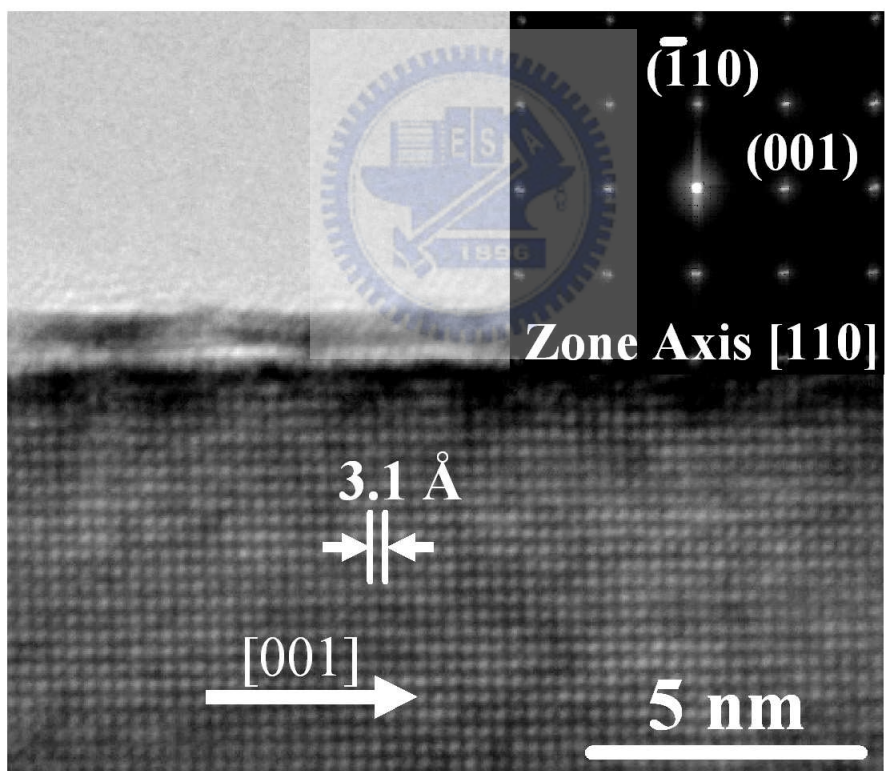
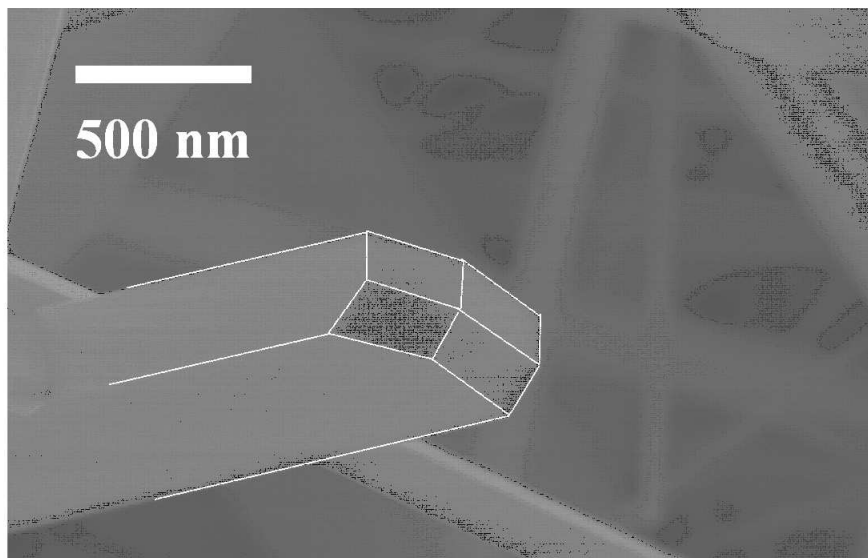


Figure 2.1: Rutile structure.



**Figure 2.2:** TEM image for a RuO<sub>2</sub> NW.

evaporation method based on the vapor-liquid-solid growth mechanism,[28] using Au nanoparticles (Ted-pella, 5–40 nm in diameter) as catalyst. A conventional quartz tube furnace was used for the synthesis. The tube was first cleaned by evacuating it to a base pressure of  $10^{-3}$  torr. Oxygen gas (99.9%) was then introduced as a carrier gas to transport the vapor produced by evaporating stoichiometric RuO<sub>2</sub> powder (Aldrich, 99.9%), which was placed in the tube center, at 920–960°C. The pressure and the flow rate of the carrier gas was 2 torr and 100 sccm, respectively. Silicon substrates with a native oxide layer on top were placed at the downstream end of the tube, where the temperature was kept at 450–670°C. Several hours later, single-crystalline RuO<sub>2</sub> NWs were grown on the substrates. The as-deposited NWs were further analyzed by using field-emission scanning electron microscopy (FE-SEM), transmission electron microscopy (TEM), x-ray diffraction (XRD), and x-ray energy dispersive spectroscopy (XR-EDS). Figure 2.2(a) shows the SEM image focused on a particular NW, of which the nearly square cross section is illustrated. The TEM image and the corresponding electron diffraction pattern are shown in Fig. 2.2(b). Detailed results of the material characterizations can be found elsewhere [15].

### 2.1.2 IrO<sub>2</sub>

Iridium dioxide, IrO<sub>2</sub>, also crystallizes in the rutile structure with the lattice constants differing from RuO<sub>2</sub> by less than  $\approx 1\%$  (see Fig. 2.1). Owing to its high resistance to the inter-diffusion of oxygen, as well as its excellent thermal and chemical stability [29], it has been used in many diverse applications. For instance, it has been investigated for use as optical switches in electrochromic devices [30], as thin film electrodes for dynamic random access memories [31], and as durable electrode materials for oxygen or chlorine evolution [32]. More recently, IrO<sub>2</sub> NWs have been studied as high-performance and robust field emitters due to their low surface work function [33].

Self-assembled single-crystalline IrO<sub>2</sub> NWs were grown onto sapphire (100) substrates via the MOCVD method, using the low-melting iridium source

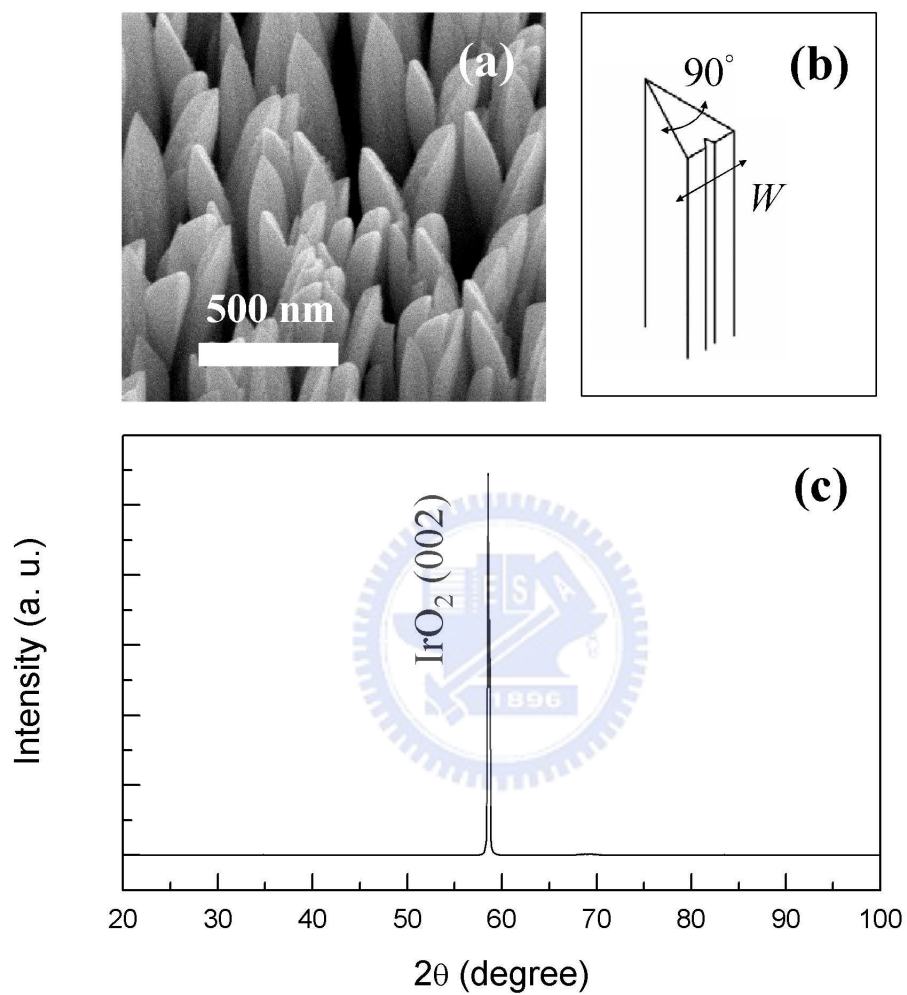


**Figure 2.3:** (a) Tilted FESEM image of as-grown  $\text{IrO}_2$  NWs revealing nearly triangular cross sections. (b) Schematic plot of the geometry for a NW. (c) XRD pattern of the NWs.

reagent (MeCp)Ir(COD) supplied by the Strem Chemicals. Both the precursor reservoir and the transport line were controlled in the temperature range of 100–130 °C to avoid precursor condensation during the vapor-phase transport. High purity oxygen, with a flow rate of 100 sccm, was used as the carrier gas and reactive gas. During the deposition, the substrate temperature was kept at 350 °C, and the chamber pressure was held at  $23\pm 1$  mbar to obtain the quasi-one-dimensional IrO<sub>2</sub> crystals. The deposition rate of NWs with nearly triangular cross sections was estimated to be 20–25 nm/min. By adjusting the temperatures of precursor reservoir and substrate, NWs with different cross-sectional morphologies, such as triangles and squares, could be obtained [34]. For the sake of convenience for resistance measurements, the NWs with nearly triangular cross sections [figures 2.3(a) and 2.3(b)] were used in this work since they have the longest length ( $\sim 3 \mu\text{m}$ ) among all morphologies. The as-deposited NWs were analyzed using field-emission scanning electron microscopy (FE-SEM), transmission electron microscopy (TEM), x-ray diffraction (XRD) and x-ray photoelectron spectroscopy (XPS). Figure 2.3(c) shows the XRD pattern of the NWs used in this work, in which the unique (002) diffraction signal indicates the nearly single-crystalline quality as obtained in our previous results [35]. Detailed fabrication processes and material characterizations can be found elsewhere [33, 34, 35].

## 2.2 Electrical measurements

Electrical contacts onto individual NWs were fabricated by the standard EBL process as described below. Figure 2.4 shows the schematic plot of the process. Silicon substrates with a  $\approx 200$ -nm thick SiO<sub>2</sub> layer on top were first photo-lithographically patterned with Cr/Au ( $\approx 10/60$  nm) macro-electrodes using bi-layer photoresist process to create reverse-slope resist sidewall profiles. Several droplets of dispersed alcoholic solution containing RuO<sub>2</sub> or IrO<sub>2</sub> NWs were dropped on the substrate. Transfer of the NWs could also be achieved by bringing the patterned Si substrate into loose surface contact with the substrate where the NWs were actually grown onto. No differences have been

found between these two methods.<sup>1</sup> Individual NWs were then positioned with SEM. A spin-coated thick layer of PMMA (polymethyl methacrylate) on top of the substrate was exposed to electron beam to produce submicron patterns. Following the thermal evaporation of Cr/Au films ( $\approx 10/90$  nm thickness,  $\approx 1/5$  Å/s deposition rate), lift-off techniques were applied to generate submicron electrodes contacting the NWs.

Copper leads were attached to the macro-electrodes with Ag paste, and the substrate was thermally anchored to the sample holder mounted with a calibrated silicon diode thermometer on a standard  $^4\text{He}$  cryostat. For measurements down to sub-Kelvin temperatures, an Oxford Heliox  $^3\text{He}$  refrigerator with a calibrated  $\text{RuO}_2$  thermometer was used.

The resistances were measured by two different methods, depending on which measurement configuration was employed. First, in order to investigate the *intrinsic* electronic properties of individual NWs, a standard four-probe (4-p) measurement configuration [Fig. 2.5(b)] was applied, using a Linear Research LR-700 AC resistance bridge. Second, for the three-probe (3-p) and two-probe (2-p) measurement configurations [Fig. 2.5(c) and (d), respectively], the resistances were measured by the DC method, in which a Keithley K-6430 source meter as a current source and a K-182 nanovoltmeter were used, and the current-reversal method [36] was adopted so that any existing thermoelectric voltages along the measurement loop were canceled. For some 2-p measurements (in which higher resistance readings were obtained), only the K-6430 source meter was used.

Obviously, in the 2-p method, the measured resistance  $R$  is the sum of the NW sample resistance  $R_s$  plus the two electronic contact resistances  $R_c$ 's and the two submicron-electrode resistances  $R_{el}$ 's, i.e.,  $R(T) = R_s(T) + 2R_c(T) + 2R_{el}(T)$ . The prefactor 2 is introduced to denote that there are two similar electronic contacts in series (and also, two similar submicron electrodes in series).<sup>2</sup> We have assumed this simple case here because they were fabricated

---

<sup>1</sup>For  $\text{IrO}_2$  NWs, only the first method was used, i.e., the wet method.

<sup>2</sup>The resistances of the submicron electrodes are similar at least within an order of magnitude, though they actually have different geometrical sizes (except their thicknesses).



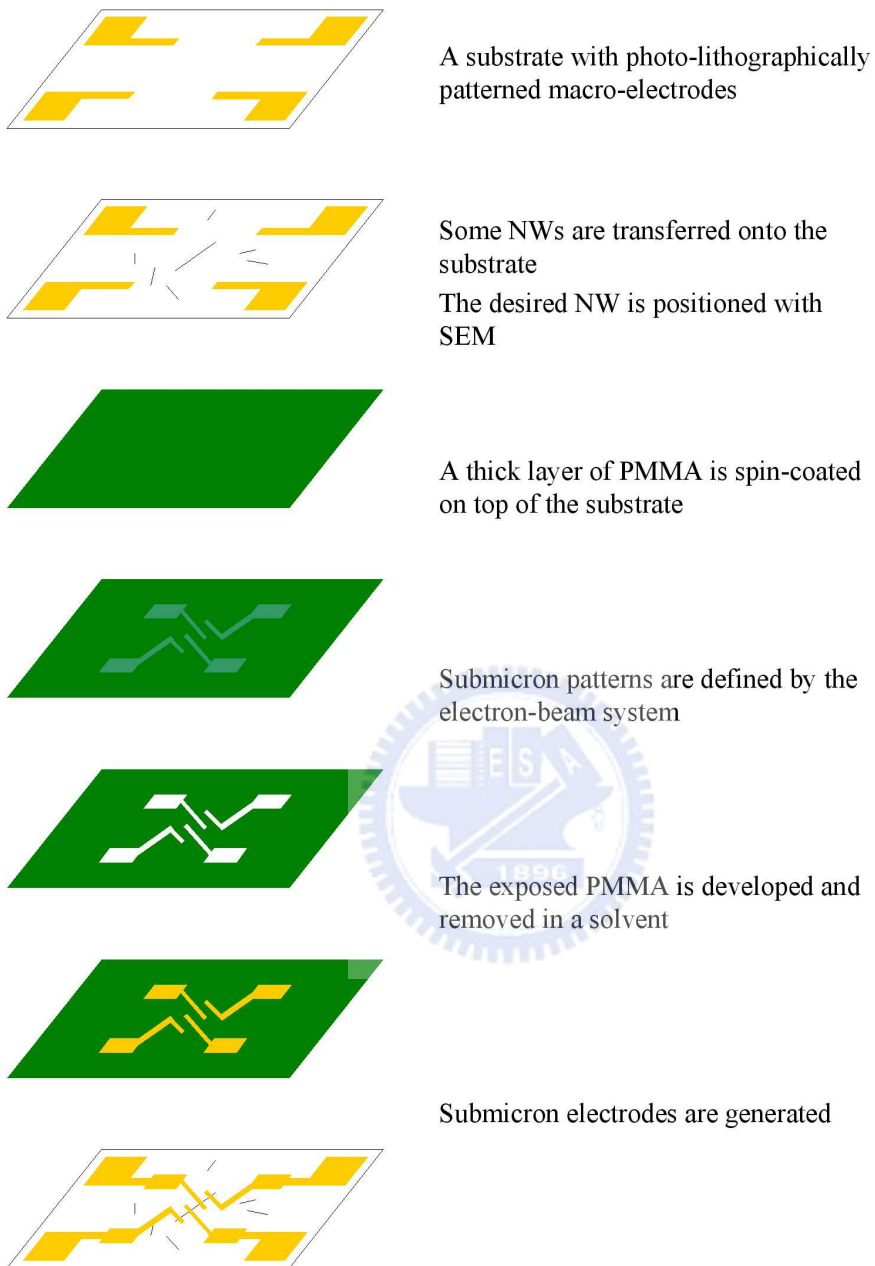


**Figure 2.4:** Schematic plot of making electrical contacts onto individual NWs.

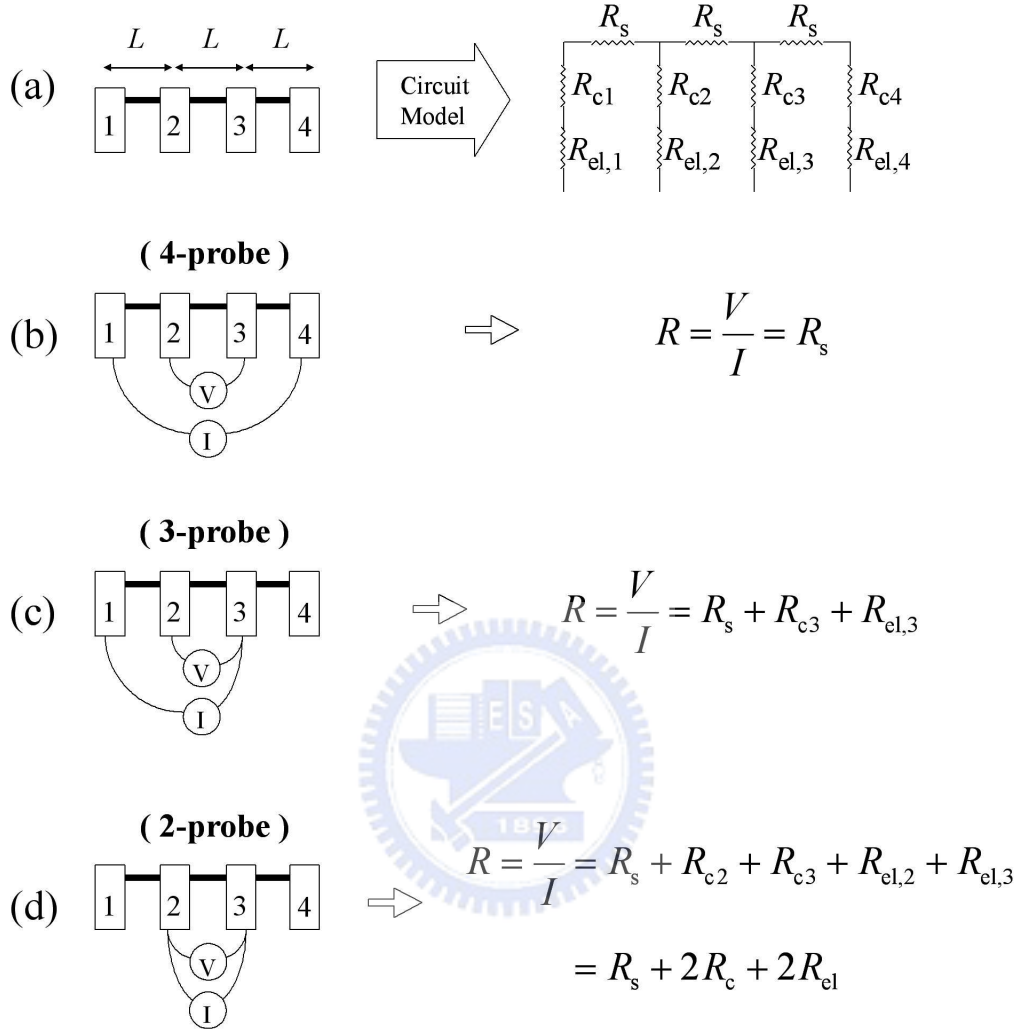


**Figure 2.5:** (a) Schematic diagram for a single NW (thick bar) with four electronic contacts on it and the equivalent circuit model.  $R_s$  denotes the resistance of each segment of the NW (i.e., the sample resistance).  $R_{c1}$ ,  $R_{c2}$ ,  $R_{c3}$  and  $R_{c4}$  denote the electronic contact resistances between the NW and the submicron electrodes 1, 2, 3 and 4, respectively.  $R_{el,i}$  denotes the submicron-electrode resistance of the  $i$ th electrode. Four-probe (b), three-probe (c) and two-probe (d) measurement configurations, and the corresponding measured resistances. In (d), the approximations  $R_{c2} \approx R_{c3} \equiv R_c$  and  $R_{el,2} \approx R_{el,3} \equiv R_{el}$  are assumed (see text).

simultaneously under the same condition and on the same NW. In the case of high-resistance electronic contacts (i.e.,  $R \gg R_s$  and  $R \gg R_{el}$ ), the  $R_c$  may dominate the measured resistance and the approximation  $R \approx 2R_c$  is valid for the whole range of experimental temperature. The measured magnitude and temperature behavior of  $R$  thus faithfully reflect the magnitude and temperature behavior of  $R_c$ . As a result,  $R_c(T)$  can be quantitatively inferred.

For the case of low-resistance electronic contacts (i.e.,  $R_c$ ,  $R_s$ , and  $R_{el}$  are similar within an order of magnitude), measurements using additional probe configurations are required to extract the resistance of each electronic contact. For example, the resistance of the sum of the two electronic contacts  $R_{c2}$  and  $R_{c3}$  in Fig. 2.5 can be obtained by subtracting the 4-p result from the result obtained from the quasi 4-p measurement configuration [Fig. 2.6(a)]. To further explicitly extract the resistance of each electronic contact, a quasi 3-p probe measurement configuration [Fig. 2.6(b)] is needed.

In the present work, only the cases of high-resistance electronic contacts are discussed.




---

Typically,  $R_{el} \approx$  several tens  $\Omega$ .

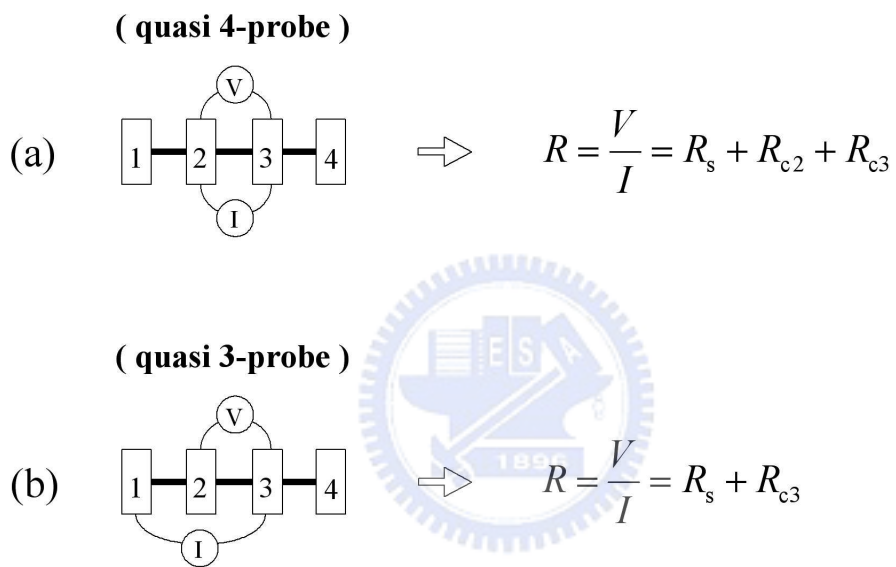


**Figure 2.6:** Additional probe configurations needed to extract the resistance of each electronic contact.

## Chapter 3

### Electronic transport in metal nanowires

#### 3.1 Introduction

Fundamental studies concerning the physical properties (e.g., electronic structures, Boltzmann transport properties, and optical properties) of  $\text{RuO}_2$  and  $\text{IrO}_2$  have been investigated for a long time, both experimentally [18, 19, 37, 38, 39, 40] and theoretically [41, 42, 43, 44, 45]. It is often accepted that the current understanding of the material is fairly complete. In particular, the electrical resistivities of  $\text{RuO}_2$  and  $\text{IrO}_2$  single crystals [18, 19] and disordered thick films [46, 47, 48] have been investigated over a wide range of temperature from 0.3 up to 1000 K. It has been shown that, for  $\text{RuO}_2$  and  $\text{IrO}_2$  single crystals, the temperature dependence of resistivity is essentially independent of the crystal orientation [18]. More specifically, the electronic conduction process in  $\text{RuO}_2$  rutile has been theoretically determined from the first-principles electronic-structure calculations and found to conform to the behavior as described by the Boltzmann transport equation [43]. Good agreement with the experiments has been established [19, 43].

#### 3.2 Theoretical background

In this section, a brief description of the electronic transport properties of  $\text{RuO}_2$  and  $\text{IrO}_2$  single crystals is given. More theoretical and experimental details can be found in Refs. [19, 43].

Originally, the temperature dependent resistivities of  $\text{RuO}_2$  and  $\text{IrO}_2$  rutile structures were explained [18] in terms of a two-band model [49], which describes the electron-phonon scattering in transition metals with parabolic  $s$  and  $d$  bands. In this model, the electrons are scattered by acoustic phonons from a Fermi sheet of high mobility and low band mass to one of low mobility and

high band mass. However, based on their first-principles electronic-structure calculations, Glassford and Chelikowsky [43] have pointed out that the Fermi surface of RuO<sub>2</sub> has no such topology, which would account for such a high degree of interband transitions between Fermi sheets. On the contrary, they gave a description of the temperature behaviour of resistivity for RuO<sub>2</sub> by including an additional contribution due to the scattering of electrons with optical-mode phonons. It has been found to agree well with the experiments [19, 43].

Theoretically, the resistivity is defined as

$$\rho = \frac{4\pi}{\Omega_p^2 \tau} , \quad (3.1)$$

where  $\Omega_p$  is the plasma frequency and  $1/\tau$  is the electron scattering rate. The  $\Omega_p$  can be theoretically calculated from a knowledge of the electronic structure of the material or experimentally determined from optical and transport measurements. If only electron-phonon scattering is taken into account, the scattering rate  $1/\tau$  can be written as

$$\frac{1}{\tau} \propto \int_0^\infty \frac{d\omega}{\omega} \alpha^2 F(\omega) \left[ \frac{\hbar\omega/2k_B T}{\sinh(\hbar\omega/2k_B T)} \right]^2 , \quad (3.2)$$

where  $\omega$  is the phonon frequency,  $\alpha^2$  is the effective frequency dependent electron-phonon coupling parameter, and  $F(\omega)$  is the phonon density of states, which can be obtained from neutron scattering data. However, no matter experimentally or theoretically, the so called “spectral function”  $\alpha^2 F(\omega)$  is difficult to get separated and normally has to be considered as a whole.

For typical metals, a Bloch-Grüneisen type behaviour which accounts for the scattering of electrons with acoustic-mode phonons is followed. This model can be obtained by replacing the  $\alpha^2 F(\omega)$  with its equivalent in the Debye approximation (where  $F(\omega) \propto \omega^2$  is assumed):

$$\alpha^2 F(\omega) \propto \lambda_{BG} \left( \frac{\omega}{\omega_D} \right)^4 \theta(\omega_D - \omega) , \quad (3.3)$$

where  $\theta$  is the step function,  $\omega_D$  is the Debye frequency (which is defined as the maximum phonon frequency), and  $\lambda_{BG}$  is the transport electron-phonon

coupling constant in the Bloch-Grüneisen model. Substituting Eq. (3.3) into Eq. (3.2) and letting  $x = \hbar\omega/k_{\text{B}}T$ , from Eq. (3.1) we have

$$\rho_{\text{BG}}(T) = \beta_{\text{BG}}T \left( \frac{T}{\Theta_{\text{D}}} \right)^4 \int_0^{\Theta_{\text{D}}/T} \frac{x^5 dx}{(e^x - 1)(1 - e^{-x})}, \quad (3.4)$$

where  $\beta_{\text{BG}}$  is a material dependent constant containing the information about  $\lambda_{\text{BG}}$  and  $\Omega_{\text{p}}$ , and  $\Theta_{\text{D}}$  is the Debye temperature corresponding to the *maximum* phonon energy in the Debye approximation of the phonon spectrum (i.e.,  $\Theta_{\text{D}} = \hbar\omega_{\text{D}}/k_{\text{B}}$ ). At higher temperatures, Eq. (3.4) results in a temperature dependence which is proportional to  $T$ , while at lower temperatures, it gives a  $T^5$  dependence.

For transition-metal oxides which contain multi-atom bases that can develop extra branches of lattice vibrations, the scattering of electrons with such optical-mode phonons should be considered as well. (In fact, for  $\text{RuO}_2$ , there exist 15 possible optical branches that the electrons can scatter from.) The contribution due to this scattering process can be obtained by replacing the  $\alpha^2 F(\omega)$  with its equivalent in the Einstein approximation (where  $F(\omega)$  is a delta function centered at the Einstein frequency  $\omega_{\text{E}}$ ):

$$\alpha^2 F(\omega) \propto \lambda_{\text{E}} \omega_{\text{E}} \delta(\omega - \omega_{\text{E}}), \quad (3.5)$$

where  $\delta$  is the delta function, and  $\lambda_{\text{E}}$  is the transport electron-phonon coupling constant in the Einstein model. Substituting Eq. (3.5) into Eq. (3.2), from Eq. (3.1) we have

$$\rho_{\text{E}}(T) = \beta_{\text{E}}T \left[ \frac{\Theta_{\text{E}}/2T}{\sinh(\Theta_{\text{E}}/2T)} \right]^2, \quad (3.6)$$

where where  $\beta_{\text{E}}$  is a material dependent constant containing the information about  $\lambda_{\text{E}}$  and  $\Omega_{\text{p}}$ , and  $\Theta_{\text{E}}$  is the Einstein temperature representing the *sole* phonon energy in the Einstein approximation of the phonon spectrum (i.e.,  $\Theta_{\text{E}} = \hbar\omega_{\text{E}}/k_{\text{B}}$ ).

Apart from the electron-phonon scattering, there is an additional term that could contribute to the temperature dependent resistivity. This is the usual electron-electron scattering which depends on  $T^2$ . It can be simply written as

$$\rho_{\text{ee}}(T) = A_{\text{ee}}T^2, \quad (3.7)$$

where  $A_{ee}$  is a material dependent constant.

According to Matthiessen's rule, these three contributions [i.e., Eq. (3.4)–(3.7)] are additive and independent of each other. The total resistivity  $\rho(T)$  is thus the sum of the residual resistivity  $\rho_0$  and Eqs. (3.4)–(3.7), i.e.,

$$\rho(T) = \rho_0 + \rho_{BG}(T) + \rho_E(T) + \rho_{ee}(T) . \quad (3.8)$$

The measured resistivity can then be fitted to Eq. (3.8), in which  $\rho_0$ ,  $\Theta_D$ ,  $\beta_{BG}$ ,  $\Theta_E$ ,  $\beta_E$ , and  $A_{ee}$  are normally regarded as adjusting parameters.

However, with so many fitting parameters, ambiguous results might occasionally occur. Fortunately, at not too high temperatures (e.g., at temperatures below 300 K)<sup>1</sup>, the resistivity due to the usual electron-electron scattering can be neglected in the first approximation because in practice in transition metals  $A_{ee}$  is only of the order of  $10^{-5} \text{ K}^{-2} \mu\Omega \text{ cm}$  [49]. Indeed, it has been shown [19] that in  $\text{RuO}_2$  single crystals fitting the experimental data without this term leads to only minor deviations of the remaining parameters (i.e.,  $\Theta_D$ ,  $\beta_{BG}$ ,  $\Theta_E$ , and  $\beta_E$ ) from those obtained by considering all the three contributions. This conclusion has also been established in other transition metals [50]. On the other hand, since in the previous studies [19, 43] the ratio of the values of  $\beta_{BG}/\beta_E$ , which determines the relative strength of the coupling of electrons with acoustic- and optical-mode phonons, was found to be  $\approx 2$ , we further assume this value in our following analysis to reduce the number of the adjusting parameters so that the more reliable results could be obtained. Nevertheless, it should be noted that to our knowledge the physics of the disorder dependence of this relative strength is still not clear yet.

To sum up, in the following analysis, the measured  $\rho(T)$  of our NWs would be fitted to the equation

$$\rho(T) = \rho_0 + \rho_{BG}(T) + \rho_E(T) , \quad (3.9)$$

in which only  $\rho_0$ ,  $\Theta_D$ ,  $\beta_{BG}$ , and  $\Theta_E$  are treated as adjusting parameters.

---

<sup>1</sup>According to their mathematical expressions, the electron-electron scattering could dominate over the other two scattering processes at temperatures below liquid-helium temperatures. Physically, this is due to the much smaller number of excited phonons because of the low-temperature (i.e., low-energy) environment.



### 3.3 RuO<sub>2</sub>

To study the intrinsic electronic transport properties of our single-crystalline RuO<sub>2</sub> NWs, the resistivities  $\rho$  as a function of temperature from 300 K down to liquid-helium temperatures for eight individual as-grown NWs were determined with the 4-p measurement configuration. Typical behaviour of  $\rho(T)$  is shown in Fig. 3.1. The physical dimensions (inspected by SEM)<sup>2</sup> and the room temperature resistivities of these NWs are listed in Table 3.1. Notice that the samples Ru-8a and Ru-8b are actually two different sections of the same NW, while the sample Ru-8ab is the sum of these two sections (see Fig. 3.2).

Clearly, the NWs reveal the electronic transport characteristic of a typical metal, i.e., the resistivity decreases as the temperature decreases from room temperature down. However, the resistivity reaches a minimum value ( $\equiv \rho_{\min}$ ) at a certain low temperature  $T_{\min}$ , below which it shows different levels of upturn for different NWs. This notable resistance rise with decreasing temperature may originate from the weak-localization and electron-electron interaction effects [51] and two-level systems [52].

Figure 3.3 shows the variation of the resistivity at  $T = 300$  K ( $\equiv \rho_{300}$ ) with diameter of the NW for the NWs measured in this work. Obviously, the plausible  $\rho_{300}$  should be  $\approx 150\text{--}300 \mu\Omega \text{ cm}$ , as obtained in Ru-1, Ru-4, and Ru-5 (whose lengths are long enough to avoid the ambiguity of the determination of the length of the NW section that we actually probed). Nevertheless, this value is still considerably higher than that ( $\approx 85 \pm 35 \mu\Omega \text{ cm}$ ) in bulk single crystals [18, 19]. Using the lowest measured  $\rho_{300} \approx 150 \mu\Omega \text{ cm}$  and the relevant material parameters for RuO<sub>2</sub> [43], we extract in our NWs the electron mean free path  $l \approx 8.4 \text{ \AA}$  and the electron mean free time  $\tau \approx 3 \times 10^{-15} \text{ s}$  at 300 K. Since this  $l$  is much shorter than the diameters of our NWs, an electron will on average have undergone several tens to few hundreds collisions (depending on the diameter and the actual  $\rho_{300}$  of the NW) within the NW before it scatters once off the NW surface. This diffusive motion of an electron implies that the

---

<sup>2</sup>To have more accurate values of the diameters, atomic force microscopy (AFM) was used to determine the diameters of the two thinnest NWs.

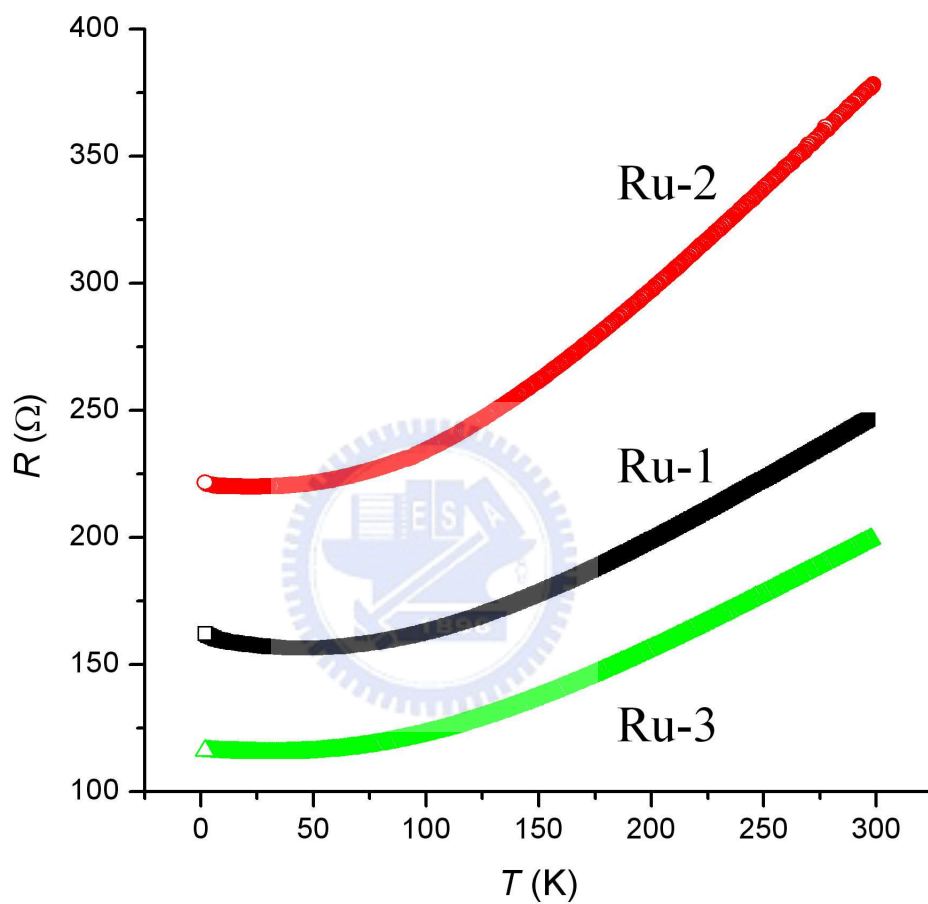


**Figure 3.1:** Typical temperature behaviour of  $\text{RuO}_2$  NWs.

**Table 3.1:** Sample parameters for the eight RuO<sub>2</sub> NWs measured by the 4-p method. Because the NWs have square cross sections, the diameter here means the side length of the square. The large uncertainties in length (defined as the length of the section that we actually probe) are mainly due to the large widths of the voltage probes and thus result in the large uncertainties in resistivity.

	Diameter (nm)	Length ( $\mu\text{m}$ )	$\rho_{300}$ ( $\mu\Omega \text{ cm}$ )	$T_{\text{min}}$ (K)	$\rho_{300}/\rho_{\text{min}}$
Ru-1	$155 \pm 5$	$4.279 \pm 0.984$	$149 \pm 43$	$\approx 45$	1.588
Ru-2	$135 \pm 20$	$1.613 \pm 0.882$	$724 \pm 523$	$\approx 22$	1.725
Ru-3	$110 \pm 4$	$1.297 \pm 0.842$	$339 \pm 234$	$\approx 32$	1.742
Ru-4	$104 \pm 12$	$3.252 \pm 0.790$	$281 \pm 125$	$\approx 42$	1.685
Ru-5	$97 \pm 13$	$9.157 \pm 0.704$	$184 \pm 61$	$\approx 43.5$	1.561
Ru-6	$76 \pm 7$	$1.593 \pm 0.862$	$825 \pm 543$	$\approx 53$	1.435
Ru-7	$55 \pm 5$	$0.670 \pm 0.441$	$483 \pm 362$	$\approx 27$	1.609
Ru-8a	$37 \pm 2$	$0.516 \pm 0.226$	$183 \pm 95$	$< 10$	1.536
Ru-8b	$37 \pm 2$	$0.516 \pm 0.226$	$158 \pm 82$	$< 10$	1.579
Ru-8ab	$37 \pm 2$	$1.032 \pm 0.226$	$141 \pm 45$	$< 10$	1.554

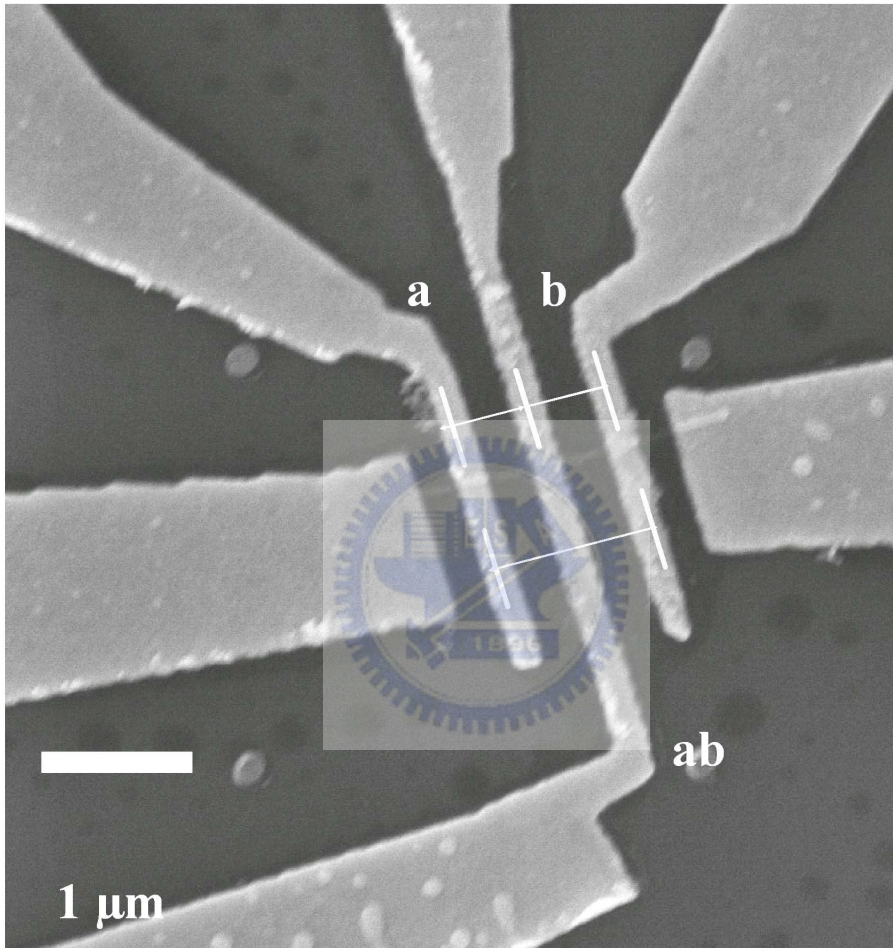


**Figure 3.2:** SEM image of the Ru-8 NW.

electronic transport properties in our NWs should be largely determined by their bulk properties while the surface effects may not be very effectual.

The residual resistivity ratio (RRR)  $\rho_{300}/\rho_0 \equiv \rho_{300}/\rho_{min} \approx 1.5\text{--}1.7$  for these NWs are found to be significantly lower, as compared with the corresponding bulk value ( $\approx 100\text{--}1000$ , depending on the quality of the crystal) [18, 19]. Such properties as the low RRR values and the short  $l$  lengths all indicate the presence of a high level of defects (most likely, point defects) in the NWs. This observation is in sharp distinction to the conclusion drawn from conventional materials characterization techniques such as XRD and high-resolution TEM [15], which often reveal very high quality atomic structure. Similar phenomenon had also been found in single-crystalline metallic NiSi NWs [7]. This observation suggests that the electronic transport measurements over a wide range of temperature can serve as a powerful probe for investigating the physics concerning the microscopic defects in nanostructures because of its sensitivity to the microscopic motions of conduction electrons with the existence of any level of randomness in the crystal.

### 3.3.1 Nanowires with diameters $\gtrsim 100$ nm

Despite the disorder nature of our NWs, we found that for the temperature behaviour above  $T_{min}$  our experimental data still can be explained within the framework of the Boltzmann transport theory for typical metals, as given in Section 3.2.

Figure 3.4 shows the log-log plot of the variation of the measured normalized resistivity,  $(\rho - \rho_0)/\rho_0$ , as a function of temperature for two NWs with diameters  $\approx 100$  nm. The solid line is the least-squares fit to Eq. (3.9). As mentioned, we merely took  $\rho_0$ ,  $\Theta_D$ ,  $\beta_{BG}$ , and  $\Theta_E$  as adjusting parameters in our fitting. The fitted values of these parameters for all NWs are listed in

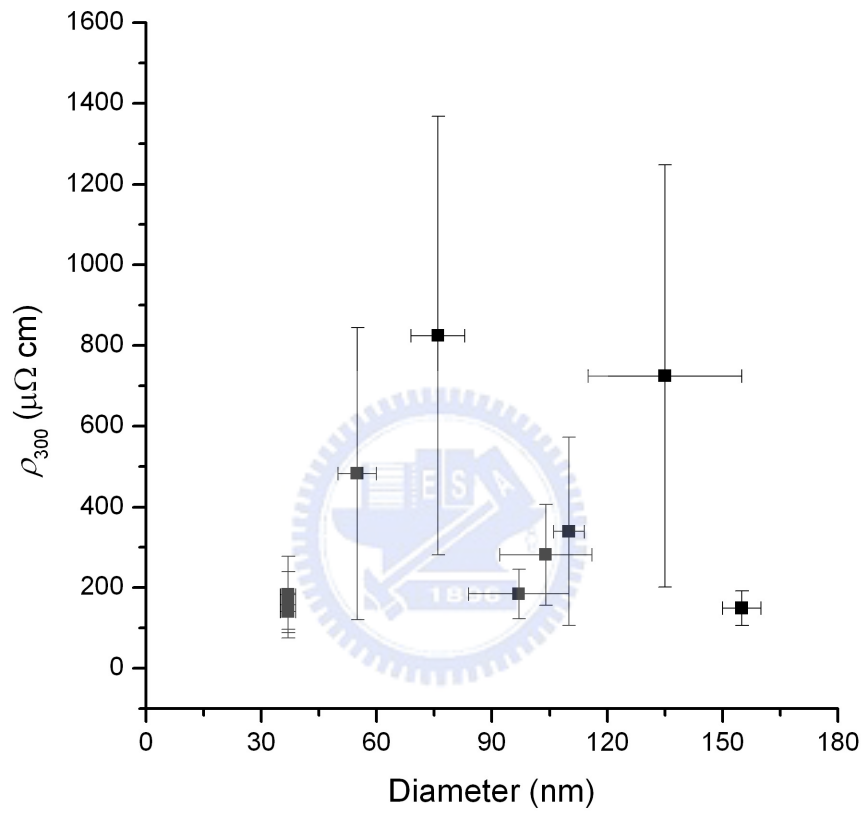


**Figure 3.3:** Variation of the resistivity at  $T = 300$  K with diameter of the NW for the NWs measured in the present work.

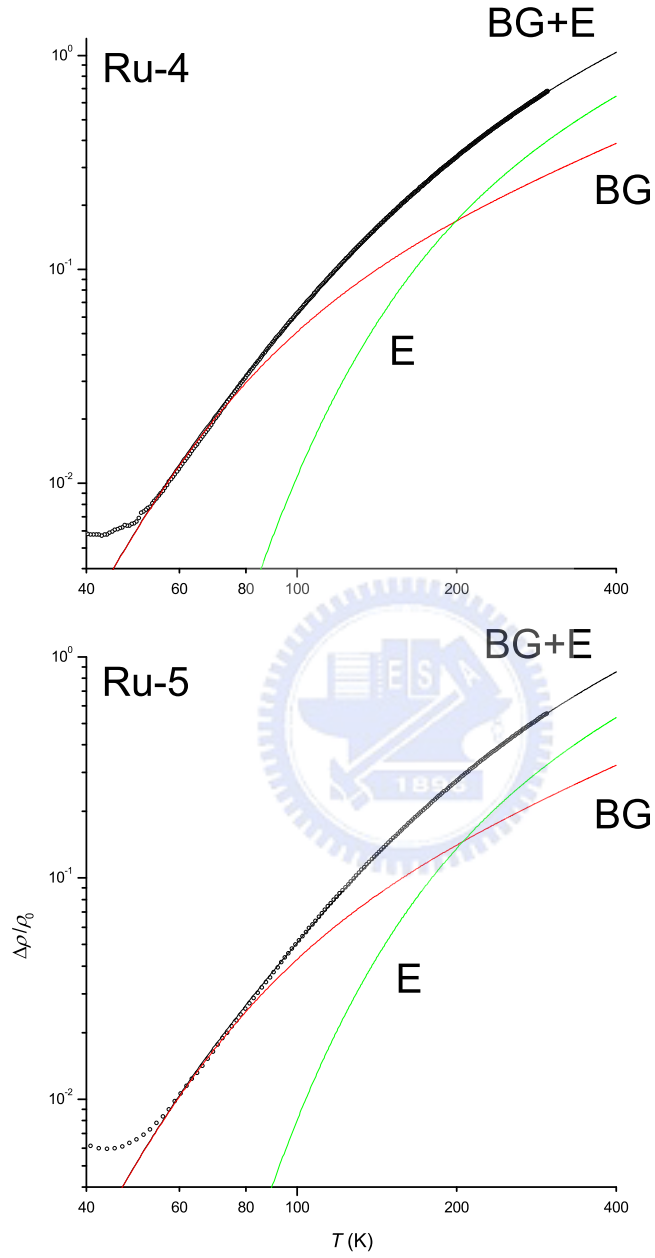


**Figure 3.4:** log-log plot of the variation of the measured normalized resistivity,  $(\rho - \rho_0)/\rho_0$ , as a function of temperature for two NWs with diameters  $\approx 100$  nm.

Table 3.2. Figures 3.5–3.8 show the variations of  $\Theta_D$ ,  $\Theta_E$ ,  $\beta_{BG}/\rho_0$ ,<sup>3</sup> and  $\rho_0$  with diameter, respectively. In this section, only NWs with diameters  $\gtrsim 100$  nm would be discussed. The results for NWs with diameters  $< 100$  nm would be discussed later.

We first notice that the fitted values of  $\Theta_D$  and  $\Theta_E$  are nearly identical for the NWs with diameters  $\gtrsim 100$  nm. However, in comparison with the corresponding bulk values ( $\Theta_D \approx 400$ – $410$  K and  $\Theta_E \approx 790$ – $810$  K) in single crystals [19, 43], we find that the  $\Theta_D$  has a value of  $\approx 400 \pm 25$  K, while the  $\Theta_E$  has a value of  $\approx 700 \pm 25$  K. A reduction of  $\approx 13\%$  in  $\Theta_E$  is observed. If we additionally set  $\Theta_D$  and  $\Theta_E$  to their bulk values (i.e., 400 and 790 K, respectively) and left only  $\rho_0$  and  $\beta_{BG}$  as free variables, we found that for all the NWs no satisfactory results could be obtained as expected. A typical best fit in this way is shown in Fig. 3.9 for the sample Ru-4.

At first glance, since we are dealing with NWs, one might conjecture that this reduction in the effective phonon characteristic temperatures results from the increased electron scattering rate with surface phonons, which are softer than bulk phonons due to the lowered coordination number of surface atoms leading to their enhanced vibrational amplitudes. Nevertheless, in our case, as mentioned above, this electron-surface scattering is less effectual, because in our NWs, the much shorter electron mean free path as compared with the diameter of the NWs makes this process much infrequent. As a matter of fact, a change in phonon related properties such as these characteristic temperatures could also be induced by some structural [53, 54], compositional [55, 56], and mechanical [57, 58] effects. For instance, in thin gold films the lowering of the effective Debye temperature is ascribed due to the electron scattering with additional surfaces created by grain boundaries [53]. However,

---

<sup>3</sup>In fact, the measured resistance  $R$  was fitted to the equation of the form:

$$\frac{R - R_0}{R_0} = \frac{\rho - \rho_0}{\rho_0} = \frac{\beta_{BG}}{\rho_0} f(\Theta_D, \Theta_E) ,$$

where  $R_0$  is the residual resistance, and  $f$  is a function of  $\Theta_D$  and  $\Theta_E$ , obtained from Eqs. (3.4) and (3.6). Therefore, the actual adjusting parameters are  $R_0$ ,  $\beta_{BG}/\rho_0$ ,  $\Theta_D$ , and  $\Theta_E$ .



**Table 3.2:** Values of the relevant parameters for the eight RuO<sub>2</sub> NWs measured by the 4-p method.

	Fit range (K)	$\rho_0$ ( $\mu\Omega$ cm)	$\Theta_D$ (K)	$(\beta_{BG}/\rho_0)$ ( $10^{-3}/K$ )	$\Theta_E$ (K)	$\rho_{300}/\rho_0$
Ru-1	55–300	$93 \pm 27$	$426 \pm 15$	$3.66 \pm 0.04$	$726 \pm 13$	1.595
Ru-2	30–300	$420 \pm 303$	$365 \pm 4$	$4.30 \pm 0.01$	$689 \pm 4$	1.725
Ru-3	40–300	$194 \pm 134$	$372 \pm 5$	$4.42 \pm 0.02$	$687 \pm 4$	1.746
Ru-4	50–300	$166 \pm 74$	$377 \pm 22$	$4.07 \pm 0.06$	$674 \pm 16$	1.695
Ru-5	55–300	$117 \pm 39$	$373 \pm 19$	$3.39 \pm 0.04$	$690 \pm 12$	1.571
Ru-6	70–300	$569 \pm 375$	$393 \pm 22$	$2.66 \pm 0.03$	$672 \pm 8$	1.449
Ru-7	35–300	$300 \pm 225$	$324 \pm 7$	$3.58 \pm 0.02$	$692 \pm 5$	1.611
Ru-8a	30–300	$119 \pm 62$	$213 \pm 13$	$3.07 \pm 0.01$	$682 \pm 2$	1.532
Ru-8b	30–300	$100 \pm 52$	$234 \pm 14$	$3.21 \pm 0.02$	$617 \pm 2$	1.585
Ru-8ab	30–300	$92 \pm 29$	$229 \pm 15$	$3.11 \pm 0.01$	$660 \pm 1$	1.542

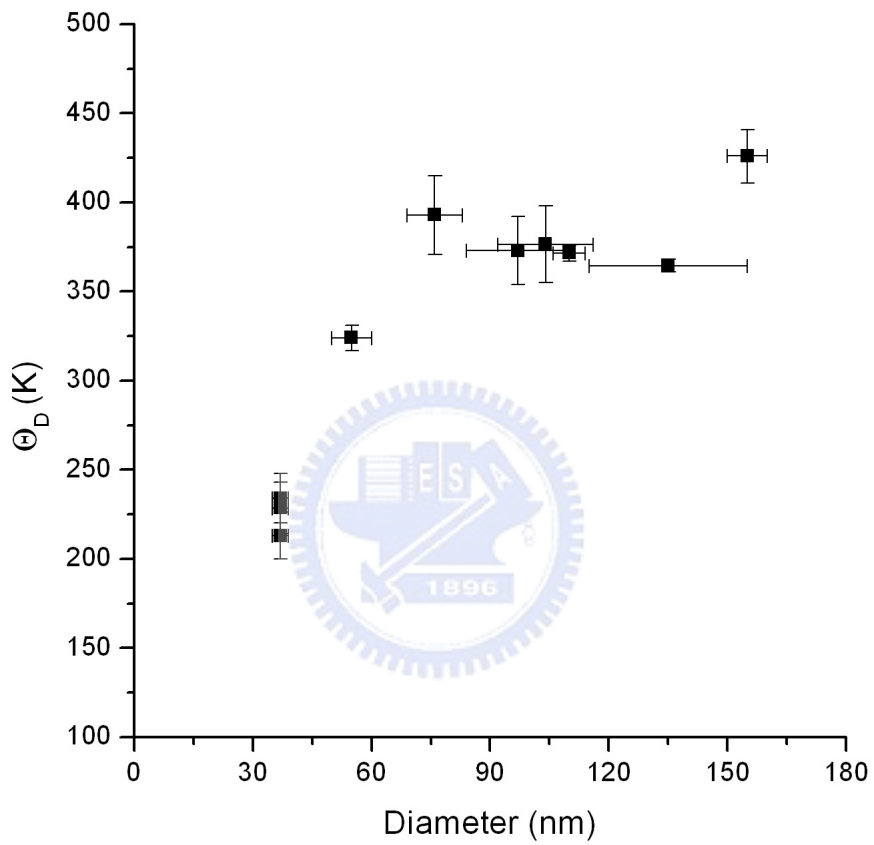


**Figure 3.5:** Variation of  $\Theta_D$  with diameter.

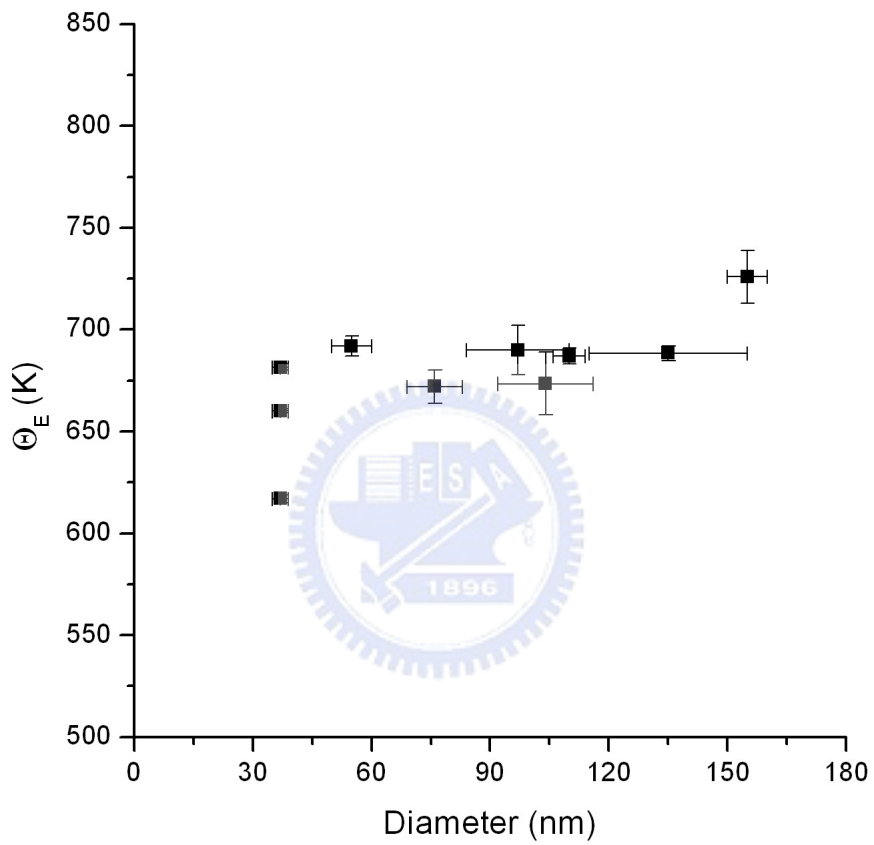


**Figure 3.6:** Variation of  $\Theta_E$  with diameter.

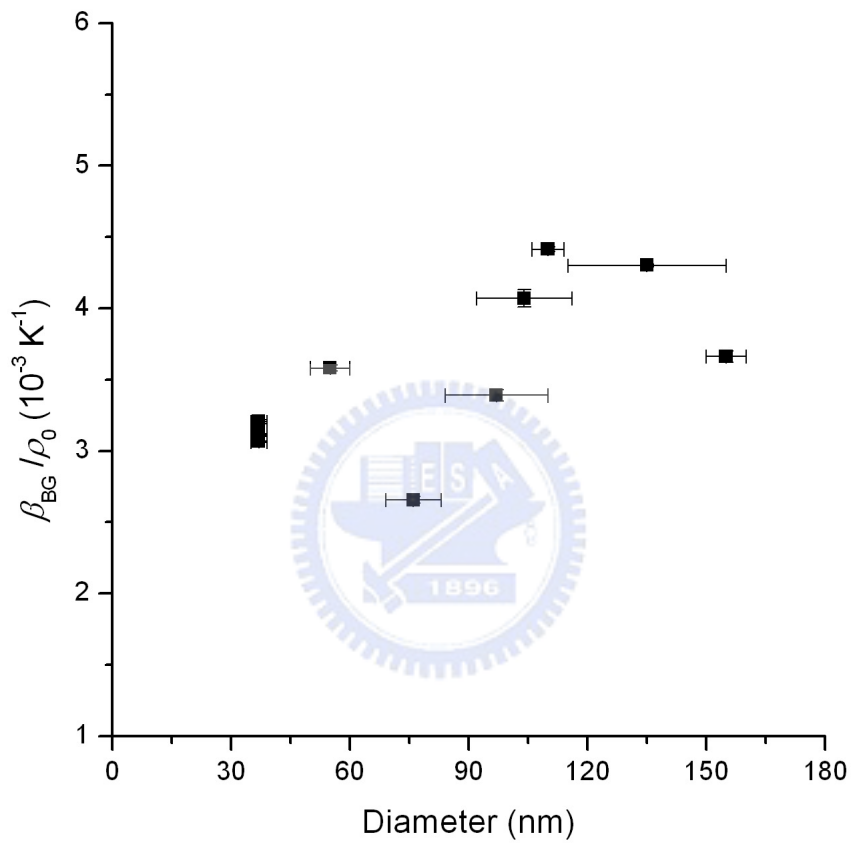


**Figure 3.7:** Variation of  $\beta_{BG}/\rho_0$  with diameter.

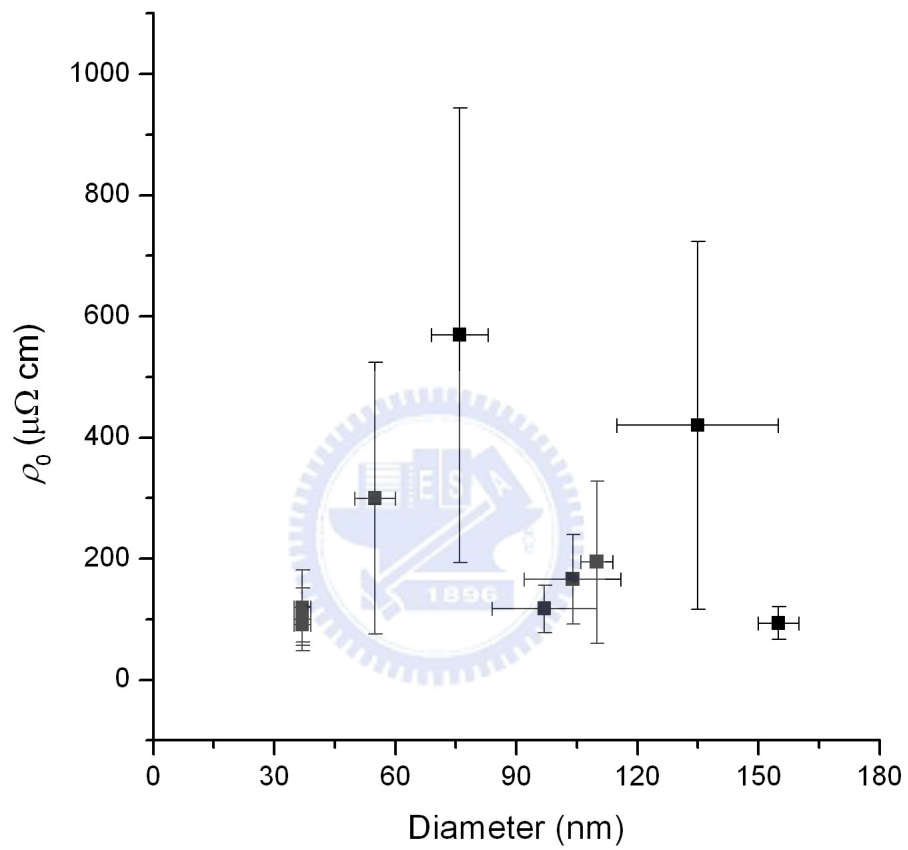


**Figure 3.8:** Variation of  $\rho_0$  with diameter.

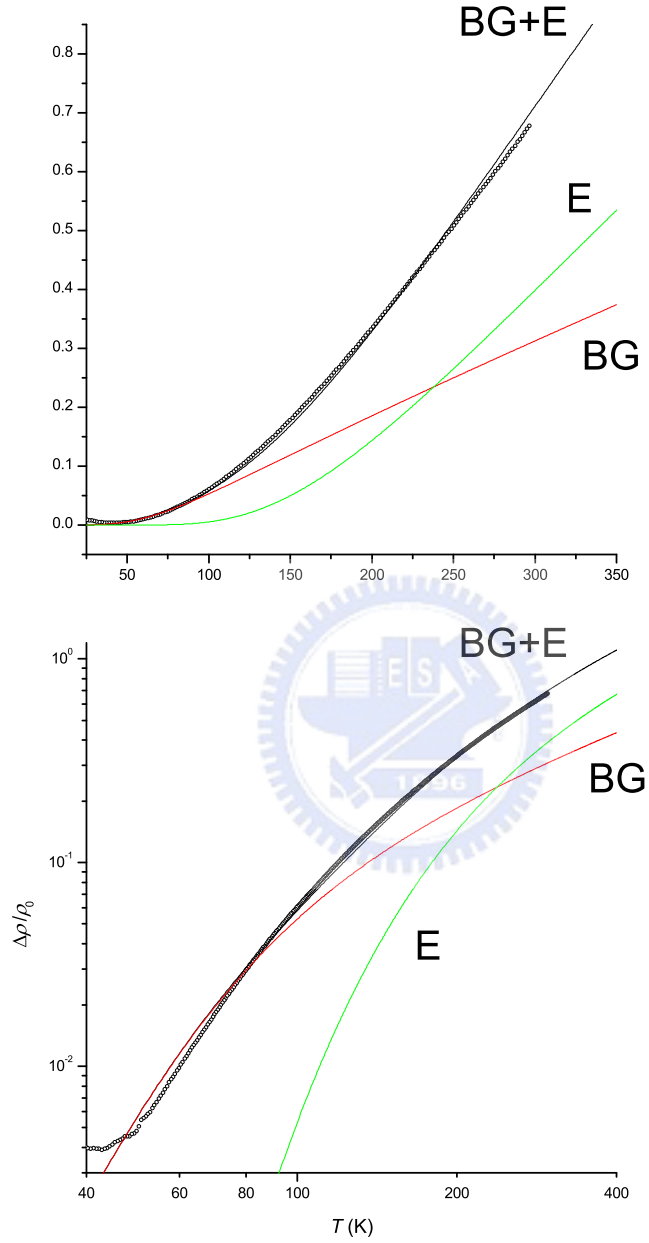


**Figure 3.9:** Best fit for the sample Ru-4 by intentionally setting  $\Theta_D$  and  $\Theta_E$  to their bulk values (i.e., 400 and 790 K, respectively) and leaving only  $\rho_0$  and  $\beta_{BG}$  as free variables.

apart from being caused by these effects, we found that in the present work another possibility could also account for the observed reduction in  $\Theta_E$  owing to the simple fact that, in our moderately disordered NWs, we interpreted the resistivity variations as arising solely from the “pure” electron-phonon scattering process that usually dominate in clean metals.

Experimentally, it has been known for a long time that deviations from Matthiessen’s rule exist in many real metals. That is, the additivity and independence which bring about Eq. (3.8) are no longer valid as the level of disorder in a metal increases. Recently, it becomes clear that such a deviation in an impure metal can be readily accounted for by merely adding an additional term into Eq. (3.8). This additional contribution was theoretically proposed and calculated by Reizer and Sergeev [59] as a consequence of the quantum interference mechanism between the elastic electron scattering and the electron-phonon scattering. It can be written as

$$\rho_{\text{int}}(T) = \beta_{\text{int}}\rho_0T^2 \int_0^{\Theta_D/T} \left[ \frac{x^2 e^x}{(e^x - 1)^2} - \frac{x}{e^x - 1} \right] dx , \quad (3.10)$$

where  $\beta_{\text{int}}$  is a material dependent constant, being independent of the amount of disorder contained in the sample. Such an “electron-phonon-impurity interference” has been experimentally demonstrated by many groups in many different material systems [48, 54, 60, 61]. It is shown that this effect can dominate the overall behaviour of  $\rho(T)$  at lower temperatures, especially at temperatures below  $\approx 0.1\Theta_D$ . However, as temperature increases, the increase of this contribution becomes less temperature dependent and finally saturates to a constant value at  $T \approx \Theta_D$ . In principle, at these higher temperatures Eq. (3.10) contributes just a small amount to the total  $\rho(T)$  (as compared with that contributed by the electron-phonon scattering) and thus can sometimes be neglected in the first approximation.

Figure 3.10 shows the result obtained by fitting the experimental data of the same NW presented in Fig. 3.9 to the equation of the form:

$$\rho(T) = \rho_0 + \rho_{\text{BG}}(T) + \rho_E(T) + \rho_{\text{int}}(T) , \quad (3.11)$$

in which we intentionally set  $\Theta_D$  and  $\Theta_E$  to their bulk values, and then left

only  $\rho_0$ ,  $\beta_{\text{BG}}$ , and  $\beta_{\text{int}}$  as adjusting parameters. In comparison with Fig. 3.9, it is clear to see that the experimental data turns out to agree quite well with the theoretical description including this additional correction.

This correction is  $\approx 6\%$  of the total resistivity at  $T \approx 400$  K. It thence slightly decreases as temperature decreases, and eventually becomes more important at temperatures approaching  $\approx 40$  K.<sup>4</sup> In fact, it is not surprising at all to have reduced values of  $\Theta_{\text{D}}$  and  $\Theta_{\text{E}}$  if we regard the measured  $\rho(T)$  as exclusively originating from the electron-phonon scattering mechanisms described by Eqs. (3.4) and (3.6). Phenomenologically, in order to compensate for lack of including Eq. (3.10), more collisions of electrons with optical and acoustic phonons accordingly had to be produced to take this accountability. At higher temperatures, the dominant behaviour of  $\rho(T)$  in this range is controlled by Eq. (3.6), in which  $\Theta_{\text{E}}$  corresponds to the unique optical phonon energy in the Einstein approximation. To offer the needed extra resisting force against the motion of electrons, the  $\Theta_{\text{E}}$  had to lower itself so that more optical phonons could be more easily excited. The environment consequently became more chaotic as seen by electrons. At last, the resistivity was compensated. Likewise, at lower temperatures, the optical phonons would quickly disappear, and the acoustic phonons thus became in this range the dominant source that the electrons could collide with. As described above, Eq. (3.4) has a temperature behaviour which crosses over from a  $T$  dependence at temperatures above  $\approx \Theta_{\text{D}}$  to a  $T^5$  dependence at temperatures approaching zero. A lower  $\Theta_{\text{D}}$  means that such a crossover would occur at relatively lower temperatures. Therefore, the  $T$  dependence would prevail over a wider range of temperature to make the needed compensation for not including Eq. (3.10), which has a weaker  $T^2$  dependence at lower temperatures.

---

<sup>4</sup>Due to the low temperature upturn in our NWs, any contribution originating from Eqs. (3.4), (3.6), and (3.10) would be masked. Without this upturn, Eq. (3.10) would dominate the temperature behaviour down to the lowest temperature until it gets masked again by the residual resistivity, as can be seen in Ref. [61].



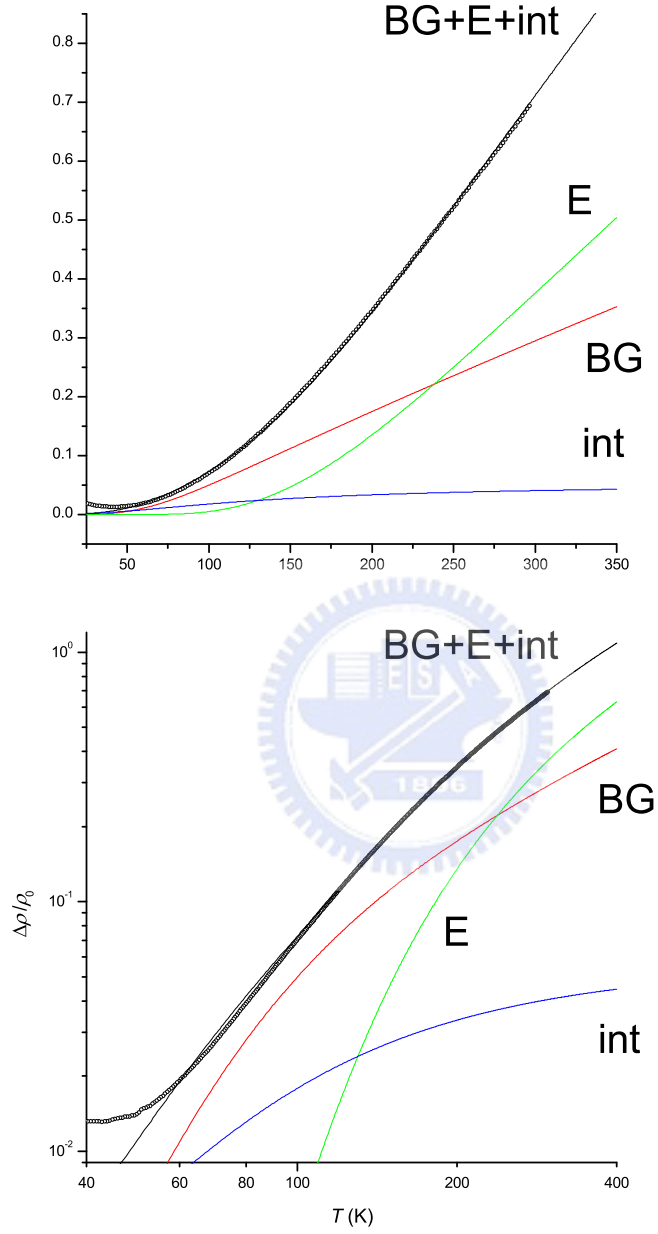


**Figure 3.10:** Best fit for the sample Ru-4 to the Eq. (3.10) by intentionally setting  $\Theta_D$  and  $\Theta_E$  to their bulk values (i.e., 400 and 790 K, respectively) and leaving only  $\rho_0$ ,  $\beta_{BG}$ , and  $\beta_{int}$  as free variables.

### 3.3.2 Nanowires with diameters $< 100$ nm

We have also measured several NWs with diameters of  $< 100$  nm. To have more accurate values of the diameters, atomic force microscopy (AFM) was used to determine the diameters of the two thinnest NWs. The measured  $\rho(T)$  was then analyzed following the model that includes only electron-phonon scattering processes given by Eqs. (3.4) and (3.6). As can be seen from Figs. 3.5 and 3.6, with decreasing diameter a more significant reduction in  $\Theta_D$  is observed while the value of  $\Theta_E$  remains barely not changed. For the thinnest NW, the  $\Theta_D$  is reduced to only one half of its corresponding bulk value.

As described in Section 3.3.1, the reduced  $\Theta_D$ , along with the reduced  $\Theta_E$ , might be conjointly caused by explaining the measured  $\rho(T)$  in terms of an incomplete model. In Figure 3.11, we show the variation of the as-obtained  $\beta_{\text{int}}$  with diameter.<sup>5</sup> The  $\beta_{\text{int}}$  is found to start increasing as diameter decreases down to a certain scale. This is actually theoretically unreasonable in the present case. According to the electron-phonon-impurity interference theory [59] leading to Eq. (3.10), the prefactor  $\beta_{\text{int}}$  is a constant for a given material, being independent of not only the amount of disorder contained in the sample but also the size of the sample, as long as the requirement of, roughly speaking,  $ql > 1$ , is satisfied, where  $q$  is the phonon wavevector and  $l$  is the electron mean free path. As will be seen in the next section, this condition is clearly obeyed for the case of our NWs. Therefore, the observed further reduction in  $\Theta_D$  can not be as well ascribed to the consequence of using a rather incomplete model.

In sum, the consequence of using an incomplete model results in only the initial reduction in  $\Theta_E$ , as described in Section 3.3.1.

#### 3.3.2.1 Size-dependent Debye temperature

As mentioned earlier, a softening of an effective  $\Theta_D$  can be ascribed to the increased number of phonon modes due to additional surface phonons that

---

<sup>5</sup>The as-obtained  $\beta_{\text{BG}}$ 's are nearly not changed. Its variation with diameter is almost the same as that in Fig. 3.7.

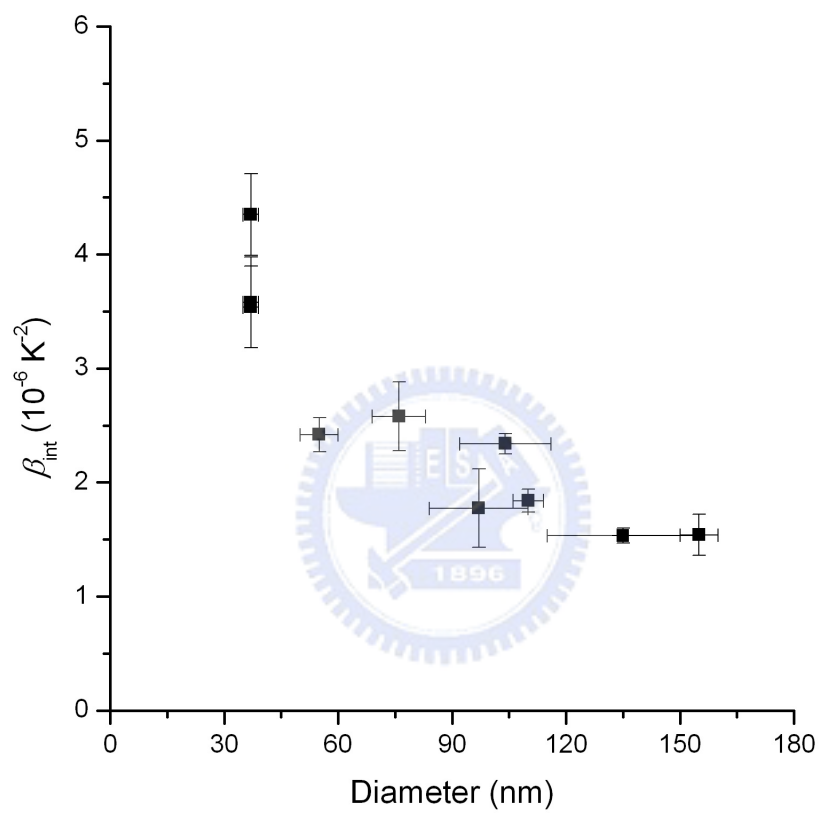


**Figure 3.11:** Variation of  $\beta_{\text{int}}$  with diameter.

electrons can scatter from. For that to be valid, an electron mean free path  $l$  comparable to the characteristic dimension of the system is certainly required. For example, in thin metallic films grown by ultrahigh vacuum molecular beam epitaxy [62], the  $\Theta_D$  was found to start deviating from the bulk value in the films of thickness below  $\approx l$ . A considerable reduction of  $\approx 50\%$  in  $\Theta_D$  was found in the thinnest film, which had a thickness approximately just one third of the  $l$ . However, in our case, the observed significant decrease in  $\Theta_D$  with decreasing diameter apparently cannot be simply explained in terms of such surface scattering because of the  $l$  being much shorter than the diameters of the NWs. Even for the thinnest one, its diameter is still several tens times longer than its  $l$ .

Obviously, we used a very simple model to describe the temperature behaviour of the resistivity in our NWs. In deriving the Bloch-Grüneisen formula, the real but complicated and barely known phonon spectral function  $\alpha^2 F(\omega)$  is replaced by a more simpler one, in which the phonon density of states having a quadratic dependence with a cutoff frequency (i.e., the Debye frequency)  $\omega_D = k_B \Theta_D / \hbar$  is used. In this Debye model, the phonon dispersion relation (spectrum) follows the form  $\omega = v_s q$ , where  $v_s$  is the sound speed of the material and  $q$  is the phonon wavevector. Although the approximation is rather crude, the Bloch-Grüneisen formula has often been found to work remarkably well when compared with experiments. However, one might still conjecture that this simplification would make serious illegitimacy if the acoustic phonon dispersion relation of the NW is substantially modified from that of its bulk as the diameter of the NW decreases down to a certain scale. The change in  $\Theta_D$  thus corresponds to an outcome that results from the application of an inappropriate and too simple model.

Indeed, spatial confinement of phonons by boundaries or interfaces of the system could render material properties like optical spectra, electrical and thermal conductivities which depend on their dynamics subject to change when one or more dimensions of the system are reduced down to the scale close to the characteristic length, such as the phonon mean free path (MFP) and the dominant phonon wavelength  $\lambda$  [63, 64]. Specifically, for acoustic phonons [63],

no significant modification in the phonon spectrum has been found in systems with the feature size  $W$  smaller than the phonon MFP. On the other hand, however, a pronounced effect on the phonon spectrum is found to occur in systems with the  $W$  further down to the scale close to or smaller than the  $\lambda$ . In fact, it has been theoretically shown [65] that such an acoustic phonon confinement effect can manifest itself by introducing not only acoustic subbands but also non-linear and considerably changed phonon dispersion relation curves at  $q$  close to the Brillouin zone center. For a free-standing nanostructure, even more complex dispersion relation curves could occur at the free surfaces due to the wave coupling of different vibrational modes [66].

The confinement effect can be roughly understood by simple means. It is known that when fundamental excitations, like phonons and electrons, are confined by the boundaries of the system, they are only allowed to exist at certain energy levels due to their wave nature. In bulk materials at temperature  $T$ , these energy levels are almost identical and basically not distinguishable from each other by experiments. As the  $W$  of the system decreases and becomes comparable with the wavelength of the excitation, the energy separation between these levels can be raised to a value larger than the thermal energy of the lattice  $k_B T$ ,<sup>6</sup> and hence becomes non-negligible and causes the related material properties to change. (Clearly, instead of reducing the  $W$ , the confinement phenomenon can as well be observed by decreasing the temperature of the system.) It is this energy “gap” that alters the total number of phonons at different levels and accordingly plays a role in possibly affecting the electron-phonon scattering rate that leads to the observed  $\rho(T)$ .

From this energy point of view, we can estimate in our NWs the temperature below which the energy separation between different phonon modes

---

<sup>6</sup>We have assumed that at temperature  $T$ , every phonon in the system has the same energy  $k_B T$ , which is in fact the exact energy of the phonon that has the occupancy of  $\approx 0.6$  if the classical Planck distribution function is obeyed. This is the same approximation often used in textbooks to obtain a qualitative explanation of the Debye  $T^3$  law for the heat capacity of solids due to lattice vibrations.

becomes appreciable. Suppose that we use a sphere in momentum space to approximate the phonon density of states,<sup>7</sup> we end up with the simple expression for the Debye temperature, which is given by

$$\Theta_D = \frac{\hbar v_s}{k_B} \left( \frac{6\pi^2 N}{V} \right)^{1/3}, \quad (3.12)$$

where  $\hbar$  and  $k_B$  have their usual meanings,  $N$  is the number of primitive unit cells in the sample, and  $V$  is the volume of the sample. In the above equation, the  $N/V$  can be approximated by  $1/a^2c$ , where  $a$  and  $c$  are the lattice constants for RuO<sub>2</sub> and equal  $\approx 4.5$  and  $3.1$  Å, respectively. Using the value of  $\Theta_D = 400$  K for bulk RuO<sub>2</sub>, we first estimate the sound speed of RuO<sub>2</sub> to be  $v_s \approx 5360$  m/s.<sup>8</sup> At temperature  $T$ , the dominant phonon in the system is approximated to have an energy  $k_B T$ . The phonon wavelength subject to the influence of changing the feature size  $W$  is  $\lambda = 2W/n$ , where  $n = 1$ . Therefore, the temperature below which the confinement effect becomes considerable is

$$T = \frac{\hbar \pi v_s}{k_B W}. \quad (3.13)$$

For the case of our thinnest NW of diameter  $\approx 37$  nm, this leads to the occurrence of perceivable energy splittings at temperatures below  $\approx 3.4$  K. This is apparently a much lower temperature range than our fit range. At temperatures higher than  $\approx 3.4$  K, many phonon modes are occupied and have almost no differences from each other. In this case, the acoustic phonon spectrum and density of states may be regarded to be Debye-like, and thus the phonon confinement effect seems very unlikely to occur in our NWs, and thus unable to account for the observed reduction in  $\Theta_D$ .

As a matter of fact, to be more specific, we shall consider the influence of acoustic phonon dimensionality on the temperature dependent resistivity directly from the point of view of the Bloch-Grüneisen formula. As we know, if there exists any influence, it would manifest itself when the  $W$  is close to

<sup>7</sup>This is the same approximation which we assume in the derivation of the Bloch-Grüneisen formula.

<sup>8</sup>This value is comparable to the speed of longitudinal sound wave in Al.

the wavelength of the dominant acoustic phonons that electrons scatter with. All we have to do is find out this dominant phonon wavelength. It should be noted that the *dominant* acoustic phonons here might not be the same ones which we concerned about in the previous paragraph. By our definition, the dominant acoustic phonons, which we refer to here, mean the acoustic phonons that contribute most to the temperature dependent resistivity, i.e., the  $\rho_{\text{BG}}(T)$  [Eq. (3.4)]. We note that, for a specimen with a  $\beta_{\text{BG}}$  and a  $\Theta_{\text{D}}$ , the largest contribution at temperature  $T$  to the integral in  $\rho_{\text{BG}}(T)$  would occur around some phonon frequency  $\omega_{\text{d}}$  which makes the integrand  $f(x)$  in Eq. (3.4) has the largest value, where  $f(x)$  has the form:

$$f(x) = \frac{x^5}{(e^x - 1)(1 - e^{-x})}, \quad (3.14)$$

and the  $x$  is given by  $\hbar\omega/k_{\text{B}}T$ . The phonons that have this vibrating frequency  $\omega_{\text{d}}$  can thus be regarded as the most important phonons in the current electron-phonon scattering process.

We plot in Fig. 3.12 the  $f(x)$  as a function of  $x$  for a material with a  $\Theta_{\text{D}}$  at several different temperatures. The shaded area denotes the integral in Eq (3.4). What particularly deserves our attention in Fig. 3.12 is that when we are at different temperatures, we have different upper limit of integration  $x_{\text{max}}$ , as indicated in the figure. Also notice that, for  $T$  larger than  $\approx \Theta_{\text{D}}/5$ , the  $f(x)$  always has the maximum value at  $x \approx 5$ . From Fig. 3.12, it can be clearly seen that the dominant phonon frequency is temperature dependent. For example, at  $T = \Theta_{\text{D}}/2$ , the maximum value of  $f(x)$  occurs right at the Debye frequency  $\omega_{\text{D}}$  (i.e.,  $\omega_{\text{d}} = \omega_{\text{D}}$ ), while at  $T = \Theta_{\text{D}}/10$ , the maximum value of  $f(x)$  occurs at the phonon frequency  $\omega_{\text{D}}/2$  (i.e.,  $\omega_{\text{d}} = \omega_{\text{D}}/2$ ).

Evidently, we can categorize them into two different groups. The first group is when we are at temperatures *above*  $\approx \Theta_{\text{D}}/5$ , at which the dominant phonon wavelength is exactly the Debye wavelength. The second group is when we are at temperatures *below*  $\approx \Theta_{\text{D}}/5$ , at which the dominant phonon wavelength is larger than the Debye wavelength, and increases as the temperature decreases.

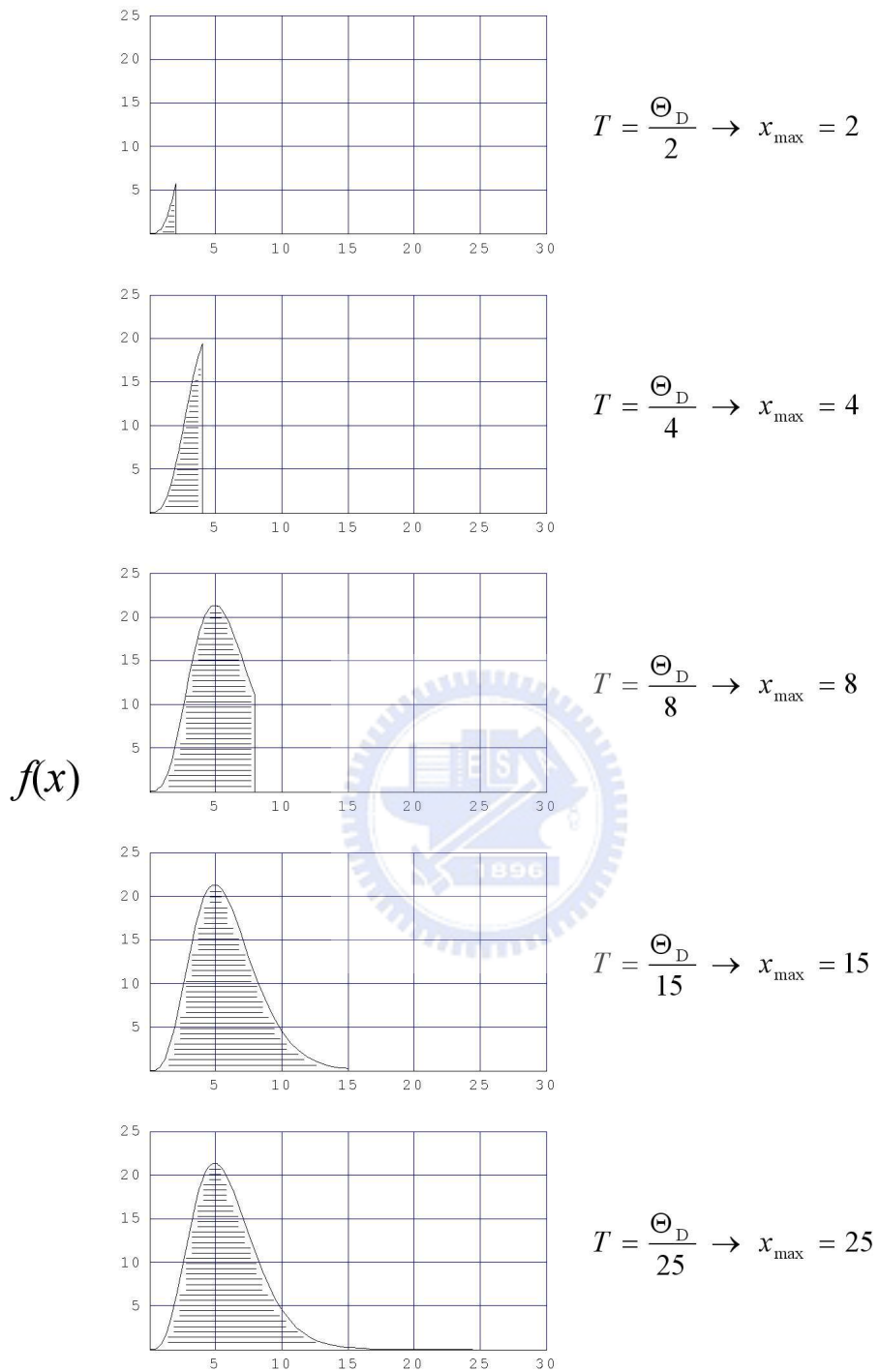


**Figure 3.12:**  $f(x)$  as a function of  $x$  for a material with a  $\Theta_D$  at several different temperatures.



From the definition of the Debye model:

$$\hbar\omega_D = \hbar 2\pi \frac{v_s}{\lambda_D} \equiv k_B \Theta_D . \quad (3.15)$$

With the use of Eq. (3.12), the Debye wavelength  $\lambda_D$  can be written as

$$\lambda_D = \left( \frac{4\pi V}{3N} \right)^{1/3} . \quad (3.16)$$

As we did previously, we can approximate the  $N/V$  by the lattice constants, and then we have, in  $\text{RuO}_2$ , the  $\lambda_D \approx 6.4 \text{ \AA}$ . Therefore, for  $\text{RuO}_2$  at higher temperatures (i.e., at temperatures above  $\approx 80 \text{ K}$  for the case of the first group), the dominant phonon wavelength  $\lambda_d (= \lambda_D \approx 6.4 \text{ \AA})$  is far below the diameter of our thinnest NW of  $\approx 37 \text{ nm}$ , and hence the phonon confinement effect is certainly not expected to occur. When the temperature decreases down to below  $\approx 80 \text{ K}$  (i.e., for the case of the second group), the dominant phonon wavelength  $\lambda_d$  starts to increase, and would, for example, have the value of  $\approx 25.6$  (128)  $\text{ \AA}$  at  $T \approx 20$  (4)  $\text{ K}$ . Accordingly, to observe any possible influence of the phonon confinement effect on the temperature dependent resistivity, we have to reduce the temperature down to at least below  $\approx 4 \text{ K}$  so that the  $\lambda_d$  would become comparable with the diameter of our thinnest NW of  $\approx 37 \text{ nm}$ . However, this is obviously not the temperature range that concerns us in our analysis.

So far, we have demonstrated that the observed significant reduction in the Debye temperature  $\Theta_D$  in our  $\text{RuO}_2$  NWs can not be satisfactorily accounted for by the quantization of the acoustic phonon spectrum that results from the phonon confinement effect, since for our experimental range of temperature, such an energy splitting, if any, can hardly make any difference to the electron-phonon scattering process in our NWs.

Other than the afore-discussed possibilities which could lead to a reduction in  $\Theta_D$ , a reduced sound speed  $v_s$  would also bring about a reduction in  $\Theta_D$ , as can be seen from Eq. (3.12) or (3.15). The sound speed is known to be a constant in a classical elastic continuum. In the Debye model for real solids, the  $v_s$  is also presumptively taken to be a constant for each polarization type,

and has the relationship:

$$v_s \propto \left(\frac{C}{M}\right)^{1/2}, \quad (3.17)$$

where  $C$  is the effective force constant between nearest neighbouring lattice planes, and  $M$  is the equivalent mass of a lattice point. Undoubtedly, the equivalent mass of a lattice point would not change with the size of a particular specimen. If the reduction in  $\Theta_D$  is truly caused by a reduced  $v_s$ , it then implies that the effective force (characterized by  $C$ ) between nearest neighbouring lattice planes might be weakened as the size of a specimen reduces down to a certain length scale. Actually, such a conjecture is not implausible at all since it has been known that the effective forces can be of quite long range, possibly up to several tens lattice planes in some materials [67]. When the size of the system reduces down to this scale, the  $C$  is accordingly prone to be affected. Indeed, the recently developed bond-order-length-strength correlation theory [68] has revealed that the broken bonds of surface atoms could make the remaining bonds between the undercoordinated atoms shorter and stronger. In a calculation [57] of Young's modulus based on this theory, the relative change in  $\Theta_D$  with decreasing size has been found, and it could be positive or negative, depending on the bond nature and the testing temperature.<sup>9</sup> The comparison has been made with the results obtained for nanoparticles. A general agreement is satisfied.

For the case of metallic NWs, a size and material dependent reduction in  $\Theta_D$  has been previously reported [69] (by using the same experimental approach as we use here), though the relative change in  $\Theta_D$  is quite small, as compared with that observed in our RuO<sub>2</sub> NWs. However, it should be noted that in Ref. [69], the measured NWs were actually embedded in a porous medium, and the possible interface interaction with the surrounding medium might further complicate the situation.

---

<sup>9</sup>Theoretically, the  $\Theta_D$  could be temperature dependent. However, in most transport studies, it is assumed and taken to be a constant independent of temperature.

### 3.4 IrO<sub>2</sub>

Figure 3.13 shows the measured resistivity  $\rho$  as a function of temperature from 300 K down to liquid-helium temperatures for two IrO<sub>2</sub> NWs with similar lateral sizes defined as  $\equiv W^2/4$ , where  $W$  is the hypotenuse as schematically depicted in Fig. 2.3(b). From inspection of the SEM images, we obtained  $W \approx 180 \pm 5$  nm for both samples. In Fig. 3.13, the symbols are the experimental data and the solid curves are the theoretical predictions (see below). Clearly, both samples reveal electrical-transport characteristic of a typical metal, i.e., the resistivities decrease as the temperature decreases from the room temperature down. However, close inspection indicates that the resistivity  $\rho(300\text{ K}) \approx 270 \pm 40 \mu\Omega\text{ cm}$  in our NWs is considerably higher than that ( $\approx 85 \pm 35 \mu\Omega\text{ cm}$ ) in bulk single crystals [19]. In addition, the resistivity ratio  $\rho(300\text{K})/\rho_0 \approx 1.1\text{--}1.2$  in our NWs is considerably lower, as compared with the corresponding bulk values ( $\approx 10\text{--}1000$ , depending on the crystal quality) [18, 19, 37], where  $\rho_0$  is the residual resistivity.

Similar with that observed in RuO<sub>2</sub> NWs, such a low residual resistivity ratio suggests the presence of a *high* level of (point) defects in our IrO<sub>2</sub> NWs. This observation is also in sharp contrast to the conclusion drawn from conventional materials characterization techniques such as XRD and high-resolution TEM [35], which often revealed seemingly high-quality atomic structure. In fact, this is exactly one of the great advantages of the electrical-transport measurements which are very sensitive to the microscopic motions of conduction electrons in the NWs.

As usual, our experimental data still can be explained in terms of the same theoretical description given in Section 3.2, despite the fact that the observed RRR in IrO<sub>2</sub> NWs are comparatively lower than those in RuO<sub>2</sub> NWs. Since the level of disorder (or, the RRR) in our NWs is similar to that in the sputtered IrO<sub>2</sub> thick films previously studied [48], the adequate formula to account for our experimental data should be thus the one described by Eq. (3.11), which would be a more complete model than Eq (3.9) for this sample.

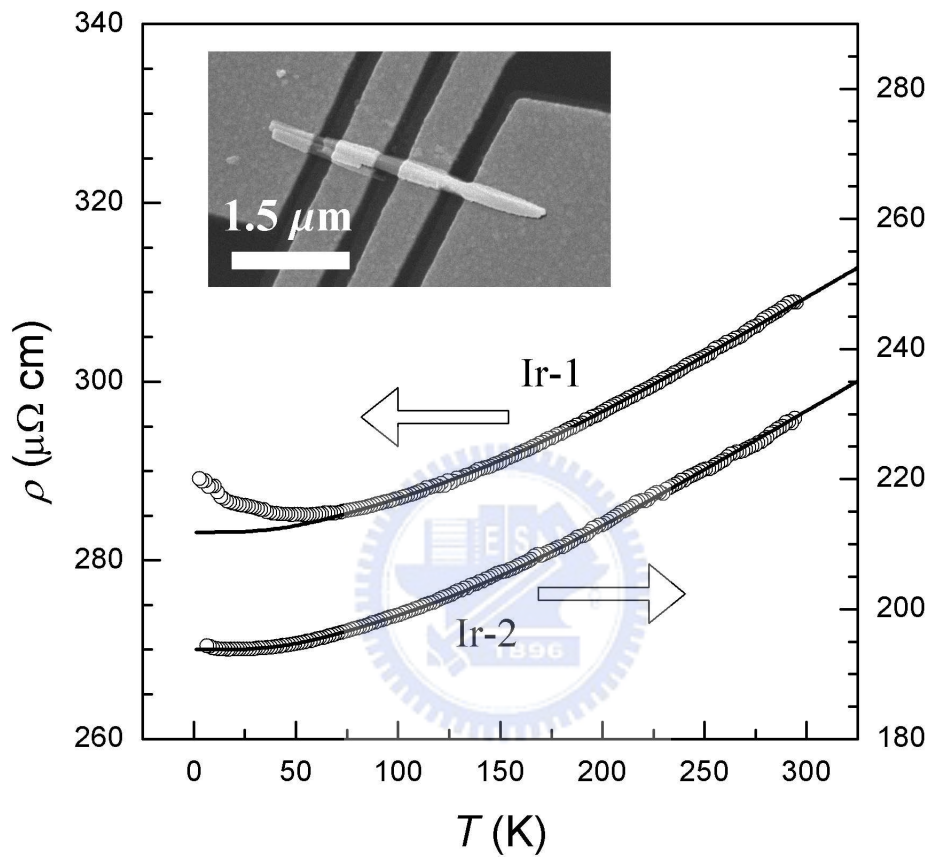


**Figure 3.13:** Resistivity as a function of temperature for two  $\text{IrO}_2$  NWs measured by the four-probe method. The symbols are the experimental data and the solid lines are the theoretical predictions of equation (3.11). The inset shows the SEM image of one NW contacted by four Cr/Au electrodes.

According to the electron-phonon-impurity interference theory [59] leading to Eq. (3.10), the prefactor  $\beta_{\text{int}}$  is a constant for a given material, being independent of the amount of disorder contained in the sample. Therefore, taking the value of  $\beta_{\text{int}} = 4.5 \times 10^{-7} \text{ K}^{-2}$  from [48], the measured normalized resistivity,  $(\rho - \rho_0)/\rho_0$ , can then be fitted to Eq. (3.9) with  $\rho_0$ ,  $\beta_{\text{BG}}$ ,  $\Theta_{\text{D}}$ ,  $\beta_{\text{E}}$  and  $\Theta_{\text{E}}$  as adjusting parameters. We find that Eq. (3.9) can well describe the resistance in the Ir-1 (Ir-2) NW between 80 and 300 K (25 and 300 K). The fitted values of the relevant parameters are listed in Table 3.3. It should be noted that the fitted values of  $\Theta_{\text{D}}$  and  $\Theta_{\text{E}}$  are nearly identical for these two samples, which in turn are close to those values obtained in the previous measurements on this material [19, 48]. However, the ratio of our fitted values of  $\beta_{\text{BG}}/\beta_{\text{E}} \approx 3.1 \pm 0.3$ , which determines the relative strength of the coupling of electrons with acoustic-mode and optical-mode phonons, is somewhat larger than the previous result ( $\approx 2$ ) [19, 48]. The relative importance of the contribution from each term in Eq. (3.9) is more clearly illustrated in a log-log plot as shown in Fig. 3.14. We point out that, below about 50 K, the resistivity of the Ir-1 NW increases more drastically than that of the Ir-2 NW as the temperature decreases. This notable resistance rise with decreasing temperature may originate from the weak-localization and electron-electron interaction effects [51] and two-level systems [52], as the sample Ir-1 possesses a higher value of resistivity than the sample Ir-2. These just mentioned disorder induced effects are not considered in Eq. (3.9).

**Table 3.3:** Values of the relevant parameters for the two IrO<sub>2</sub> NWs measured by the 4-p method. For both samples,  $W \approx 180 \pm 5$  nm and  $L \approx 0.83 \pm 0.01$   $\mu$ m. The uncertainties in resistivities mainly arise from the uncertainties in the dimensions of the NWs.

	$\rho_{300}$ ( $\mu\Omega$ cm)	$\rho_{300}/\rho_0$	$\Theta_D$ (K)	$\beta_{BG}$ ( $\mu\Omega$ cm/K)	$\Theta_E$ (K)	$\beta_E$ ( $\mu\Omega$ cm/K)	$\beta_{BG}/\beta_E$
Ir-1	$295 \pm 20$	1.09	320	0.204	840	0.071	2.87
Ir-2	$220 \pm 15$	1.19	310	0.341	820	0.099	3.44



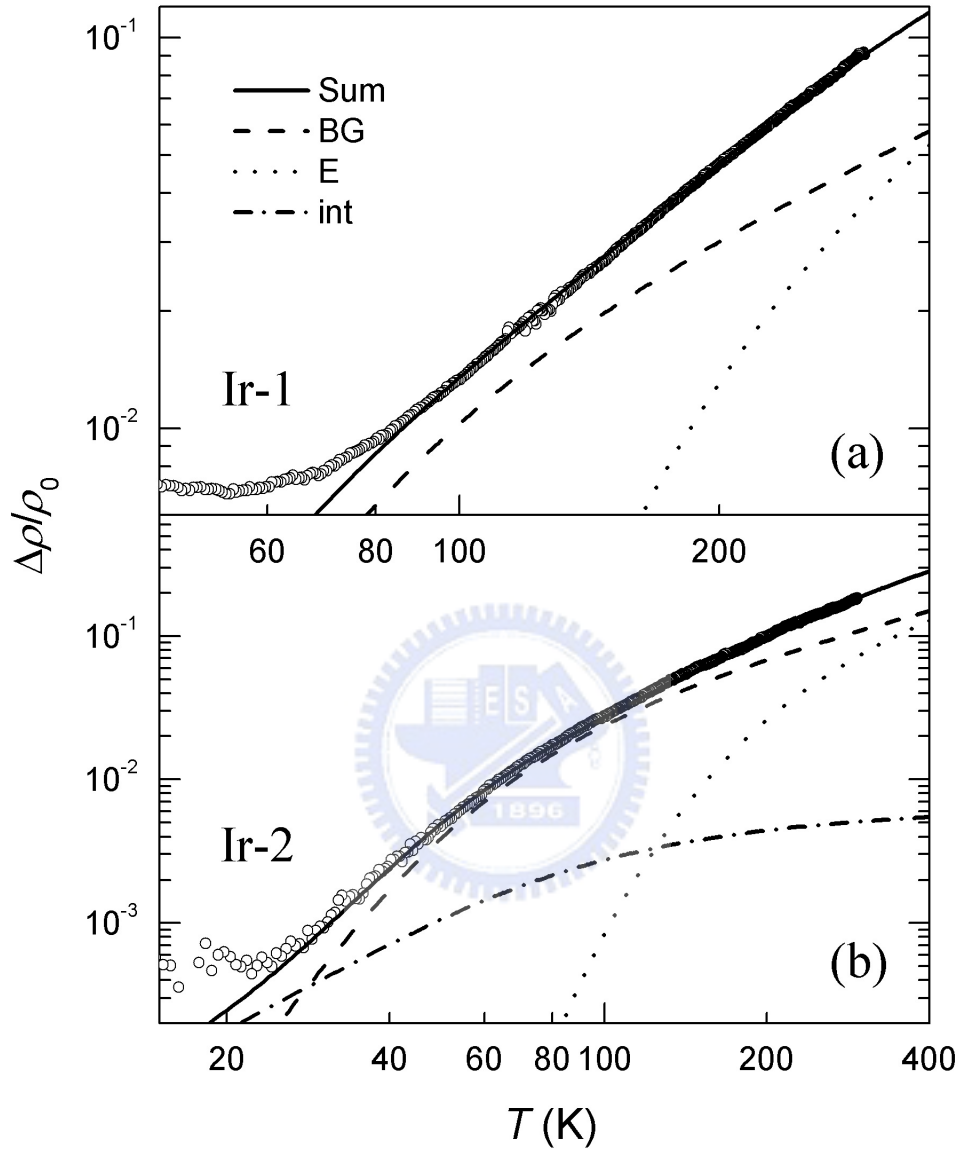


**Figure 3.14:** Log-log plot of the variation of the normalized resistivity  $\Delta\rho/\rho_0 = (\rho - \rho_0)/\rho_0$  with temperature for the two IrO<sub>2</sub> NWs studied in figure 3.13. Notice that the scales of the axes are different in (a) and (b). The contribution from the  $\rho_{\text{int}}/\rho_0$  term in the Ir-1 NW has the same magnitude as that ( $\sim 10^{-3}$ ) in the Ir-2 NW, and thus is outside the range displayed in (a).

# Chapter 4

## Electronic transport through metal nanowire contacts

### 4.1 Introduction

Nanoscale materials are important for fundamental researches and applications due to their promising potential for both new physics and technology. One major motivation for studies on self-assembled Q1D metallic NWs is their potential use as interconnects in the future nanoelectronics. Probing the electronic transport properties of these nanostructures thus becomes the very key step for the realization of numerous novel applications. Usually, connections of the instruments to the individual nanodevices are accomplished by the nanofabrication techniques such as the electron-beam lithography (which we adopted in this work) and the focused ion beam deposition method. However, a critical hindrance is that the often obtained non-negligible temperature dependent contact resistances<sup>1</sup>  $R_c$  are prone to complicate the experiments and could seriously mislead the physical interpretation of the data. Therefore, in this context, the main theme of this section – uncovering the physics and mechanism of the electronic nanocontact resistances – could provide indispensable information and valuable solution for this problem.

From the experimental point of view, the lead resistances and the electronic contact resistances in electrical measurements must be small to minimize thermal noises. Usually, the  $R_c$  of a macroscopic metal-metal contact is on the

---

<sup>1</sup>The large contact resistance ( $\approx$  tens  $k\Omega$ ) may result from a thin, dirty insulating layer incidentally formed at the interface between the submicron electrodes and the NW. This insulating layer could be the lightly contaminated or oxidized metals introduced during the electrode evaporation, the amorphous coating resulting from the complex growth process, the vacancies caused by dramatic surface roughness near the contact region, or the breaking induced by tensile stress.



order of  $\sim 1 \Omega$ . As the area of electronic contact shrinks, the magnitude of  $R_c$  may increase considerably. Moreover, it has been pointed out that, as the nanoscale being approached, the detailed atomic structure of the contact could affect the  $R_c$  significantly in fairly different manners [70].

In our case, the electronic contact resistances formed between the EBL-patterned electrodes and the NWs normally fall between several tens and several hundreds  $\Omega$ , and are not much dependent on temperature. However, highly resistive electronic contacts with room temperature resistances of order several  $k\Omega$  or higher may also be obtained in many fabrications. Figure 4.1 shows three diverse temperature behaviours of the measured resistance  $R$ , as determined from the 2-probe measurement configuration [see Fig. 2.5(d)]. As we discussed in Section 2.2, the behaviour in Fig. 4.1(c) is obviously a result of having comparable values of  $R_c$ ,  $R_s$ , and  $R_{el}$ . In the case of having high-resistance electronic contacts (i.e.,  $R_c \gg R_s$  and  $R_c \gg R_{el}$ ), the  $R_c$  may dominate the measured resistance [as shown in Fig. 4.1(a)] and the approximation  $R \approx 2R_c$  is valid for the whole range of experimental temperature. In this case, the measured magnitude and temperature dependence of  $R$  thus faithfully reflect the magnitude and temperature dependence of  $R_c$ .<sup>2</sup>

In the following sections, only the behaviour of high-resistance  $R_c$  [i.e., the one in Fig 4.1(a)] will be quantitatively discussed. We will demonstrate that the temperature dependence of  $R_c$ , could be well understood in terms of two existing phenomenological theories, one for  $\text{RuO}_2$  NWs, and one for  $\text{IrO}_2$  NWs. Such a difference may arise from the different surface conditions of different kinds of NWs (such as different surface stresses). However, we believe that either mechanism could occur even for the same kind of NWs, though the evidences supporting our conjecture have not been obtained yet.

---

<sup>2</sup>For the case of Fig. 4.1(b), since the total resistance of the Cr/Au electrodes is typically  $\approx$  few tens  $\Omega$  and the NW resistance is typically  $\approx$  few hundreds  $\Omega$ , the temperature behaviour is therefore a result of the competition between  $R_c$ ,  $R_s$ , and  $R_{el}$ . At higher  $T$ , the temperature dependence is primarily caused by the metallic properties of  $R_s$  and the  $R_{el}$ , while at lower  $T$ , the  $R_c$  dominates because of its insulating nature.

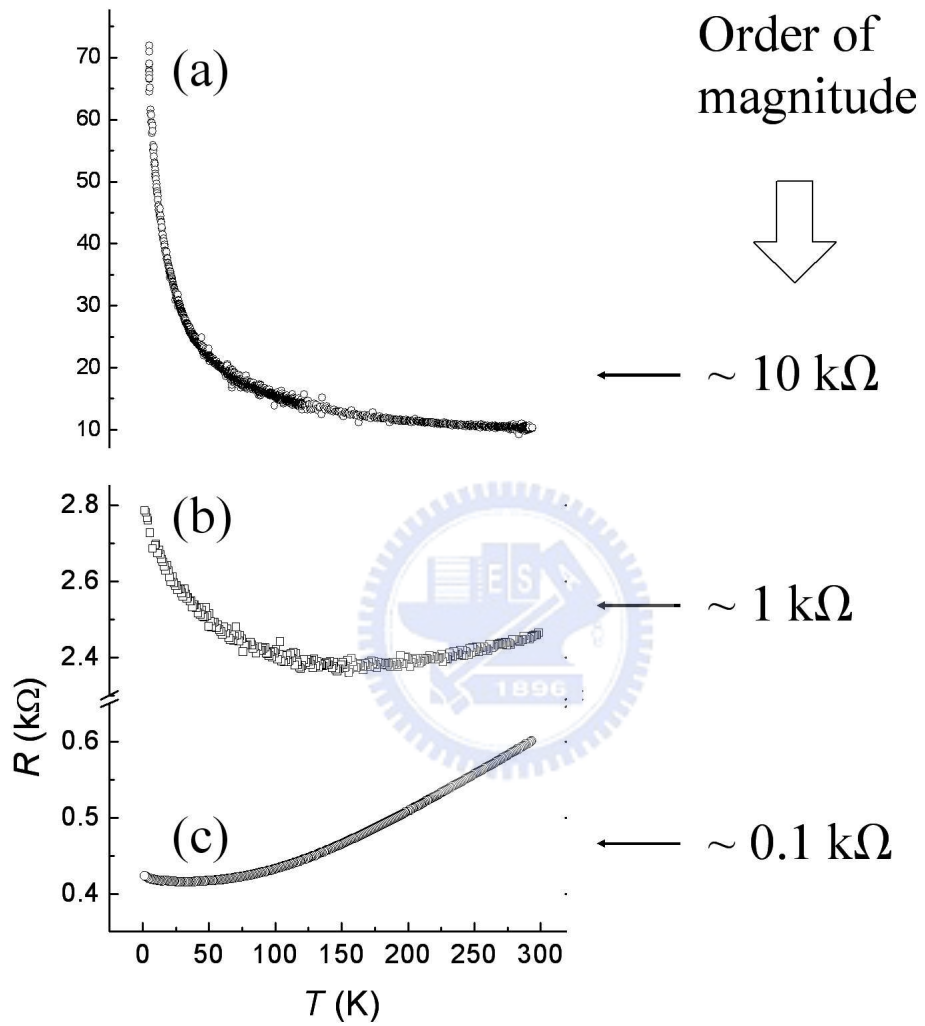


**Figure 4.1:** Three typical temperature behaviours of the measured resistance  $R$ , as determined from the 2-p method.

## 4.2 RuO<sub>2</sub>

### 4.2.1 Fluctuation-induced tunneling conduction

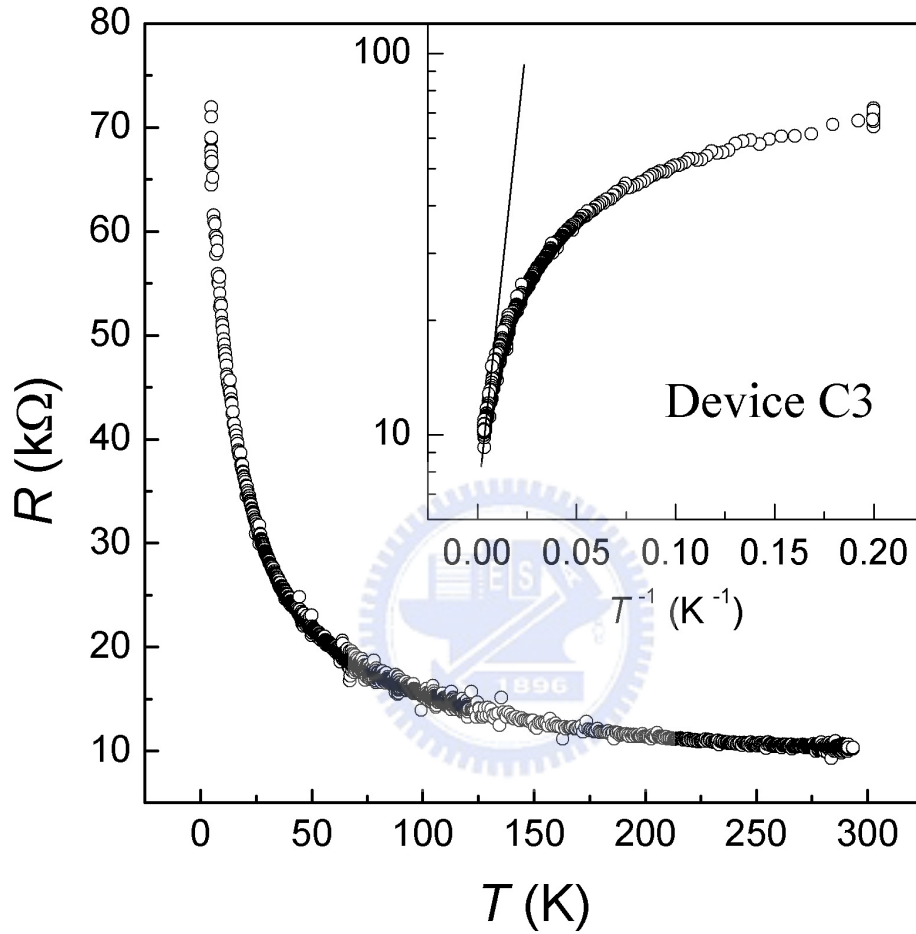
With the metallic nature of our individual RuO<sub>2</sub> NWs being established, we can already safely use these NWs to study the electronic contact resistances  $R_c(T)$  in lithographic-contacting nanostructures, using the 2-probe method.

Figure 4.2 shows the typical temperature behavior of  $R_c$  for such a high-resistance contact from 300 K down to liquid-helium temperatures, as determined from the 2-probe method on a RuO<sub>2</sub> NW. In strong contrast to the 4-probe results previously studied, now the measured resistance reveals semi-conducting or insulating behavior, i.e., the resistance increases rapidly with decreasing temperature.

The inset to Fig. 4.2 shows the variation of  $\log R$  with  $T^{-1}$  for the same device. This figure indicates that the simple thermally activated conduction (the straight solid line) is only responsible near room temperatures. As the temperature reduces from room temperature, the resistance does not increase as fast as would be expected from the thermal activation process. At liquid-helium temperatures, the resistance appears roughly constant, i.e., independent of temperature. Such a temperature independent resistance at liquid-helium temperatures can signify a conduction mechanism characteristic of simple *elastic tunneling*. Indeed, quantitative analysis (see below) indicates that the overall temperature behavior of the contact resistance can be well interpreted in terms of a tunneling conduction model. Previously, in order to explain the electrical-transport properties in certain classes of granular metal-dielectric composites, Sheng and coworkers [71, 72] have proposed a thermally “fluctuation-induced tunneling” (FIT) model, where the thermal effects arising from the capacitance  $C$  of a *small* junction formed between two *large* metal grains was considered.

According to Sheng and coworkers [71, 72], the temperature dependent resistance for small applied electric fields across a single small junction can be expressed as

$$R(T) = R_0 \exp\left(\frac{T_1}{T_0 + T}\right), \quad (4.1)$$



**Figure 4.2:** Resistance as a function of temperature for two high-resistance contacts in series, as determined from the 2-probe method on the NW device C3 (see Table 4.1). The inset shows a plot of  $\log R$  versus  $T^{-1}$  for the same NW device. The straight solid line indicates the thermal activation conduction.

where  $R_0$  is parameter which depends only weakly on temperature, and  $T_1$  and  $T_0$  are characteristic temperatures defined as

$$T_1 = \frac{8\varepsilon_0}{e^2 k_B} \left( \frac{AV_0^2}{w} \right), \quad (4.2)$$

and

$$T_0 = \frac{16\varepsilon_0 \hbar}{\pi(2m)^{1/2} e^2 k_B} \left( \frac{AV_0^{3/2}}{w^2} \right), \quad (4.3)$$

where  $\varepsilon_0$  is the vacuum permittivity,  $\hbar$  is the Planck's constant divided by  $2\pi$ , and  $m$  is the electron mass. In Eq. (4.1),  $T_1$  can be regarded as a measure of the energy required for an electron to cross the potential barrier between the two conducting regions, and  $T_0$  is the temperature below which the fluctuation effects become insignificant, since, at  $T \ll T_0$ , Eq. (4.1) is temperature independent and reduces to an expression for the expected simple elastic tunneling. In the derivation of Eq. (4.1), the conduction was first modeled [71] as the tunneling of electrons through a single potential barrier of width  $w$ , height  $V_0$ , and junction area  $A$ . ( $A$  is the size at the point of the two large conducting regions' closest approach.) If  $A$  is small enough, it was found [71, 72] that the potential barrier seen by the electrons could be effectively narrowed and lowered by the thermal voltage fluctuations ( $\approx \sqrt{k_B T / C}$ , where  $k_B$  is the Boltzmann constant) across the insulating gap due to the small effective capacitance of the junction. Such a potential-barrier modulation effect greatly influences the tunneling probability in the low temperature limit, and consequently introduces a characteristic temperature behavior to the normally temperature independent tunneling conductivity (i.e., the elastic tunneling regime).

In the case of granular composites of macroscopic sizes, it was then argued [72], via the effective-medium theory, that in a network of independently fluctuating tunnel junctions with different values of  $T_1$  and  $T_0$ , the conductivity of the network could still be well described in terms of a single junction with a representative set of  $T_1$  and  $T_0$ .

Figure 4.3 shows a plot of our experimental results in double logarithmic scale for four representative NW devices having high contact resistances (as determined from the 2-probe method). The symbols are the experimental data

and the solid curves are the least-squares fits to Eq. (4.1), with  $R_0$ ,  $T_1$  and  $T_0$  as the adjusting parameters. Inspection of Fig. 4.3 clearly indicates that the Eq. (4.1) can well describe the *overall* temperature behavior for a *wide* range of temperature between 2 and 300 K. The values of  $T_1$  and  $T_0$  can then be reliably extracted. Furthermore, by using SEM and/or AFM, we can directly measure the diameter and the length of our NWs, as well as the width of the relevant submicron Cr/Au electrodes overlying the NW. Therefore, the junction area  $A$  which appeared in Eqs. (4.2) and (4.3) is *independently* determined. (The junction area  $A$  is given by the product of the NW diameter and the width of the overlying submicron electrode.) With the values of  $T_1$ ,  $T_0$  and  $A$  being determined, the microscopic parameters characterizing the electronic contacts, i.e., the width  $w$  and height  $V_0$  of the potential barrier, may then be inferred. Our experimental values of the relevant parameters are listed in Table 4.1. Notice that, in Table 4.1, the measured resistance  $R(300\text{ K})$  for each NW device is at least an order of magnitude higher than the intrinsic resistance of the NW,  $R_s(300\text{ K})$ , justifying our approximation  $R(T) \approx 2R_c(T)$ . Moreover, the resistance ratio  $R(T)/R_s(T)$  increases rapidly as the temperature decreases below room temperature.

It should be noted that, in the FIT model, because the two conducting regions remain large in size, the charging energy  $E_c$  needed to transfer an electron from one conducting region to the other is completely negligible, i.e.,  $E_c \ll k_B T$ . This situation is very different from that in the case of Coulomb blockade which involves fine metal grains or quantum dots, where the charging energy  $E_c (\gg k_B T)$  rather than the thermal voltage fluctuations plays the crucial roles in controlling the electronic transport properties. In the present work, the volume of our “long” NW is relatively large as compared to the sizes of the fine metal grains (e.g.,  $\sim 10^3\text{ nm}^3$ ) used in Coulomb blockade studies.[73] The typical volume of our NWs is  $\sim 100\text{ nm} \times 100\text{ nm} \times 3\text{ }\mu\text{m}$ . Thus, our NW can be envisioned as a large conducting region separated by an insulating layer from another large conducting region (the submicron Cr/Au electrode) with a junction area  $A$  ( $\sim 100 \times 500\text{ nm}^2$ ). This size of  $A$  is already small enough to render the aforementioned thermal voltage fluctuations important while large

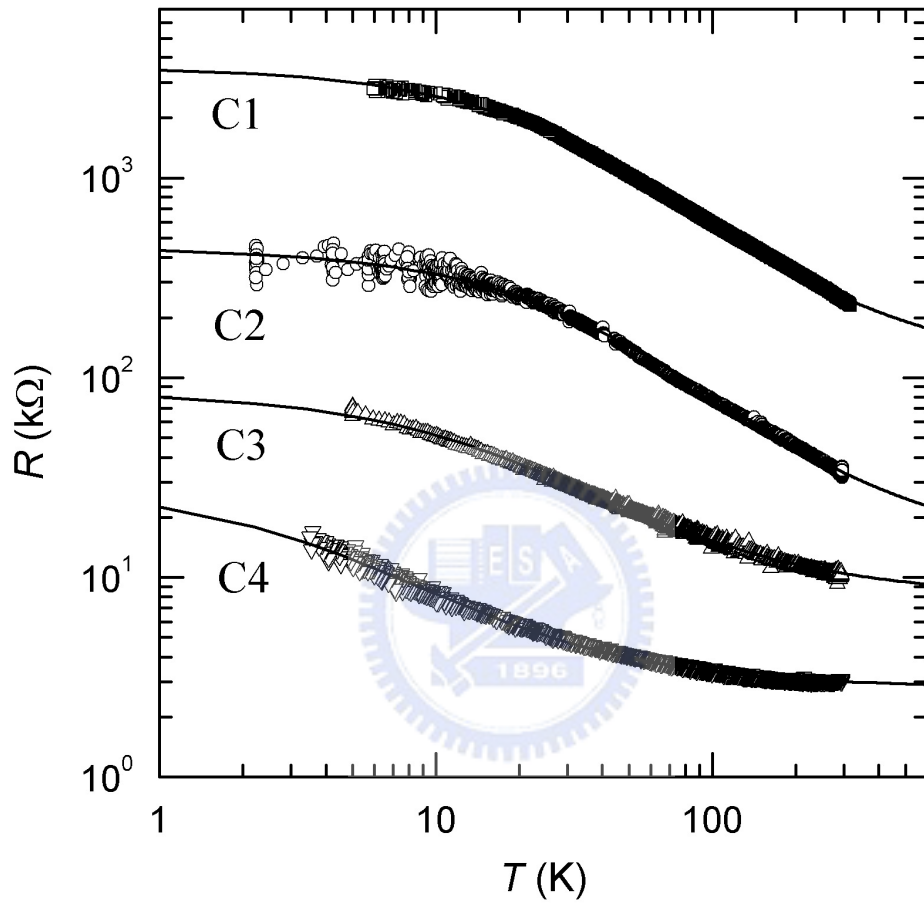


**Figure 4.3:** Double logarithmic plot of the resistances versus temperature for four high-resistance NW devices, as determined from the 2-probe method. The symbols are the experimental data and the solid curves are the theoretical fits to Eq. (4.1).

**Table 4.1:** Values of relevant parameters for four high-resistance NW devices, as determined from the 2-probe method. For each device, the NW resistance  $R_s(300\text{ K})$  was estimated from the 4-probe method, while the junction area  $A$  was determined from the SEM image.

	$R(300\text{ K})$ (k $\Omega$ )	$R_s(300\text{ K})$ (k $\Omega$ )	$R_0$ (k $\Omega$ )	$T_1$ (K)	$T_0$ (K)	$A$ ( $\mu\text{m}^2$ )	$w$ (nm)	$V_0$ (meV)
C1	241	0.67	112	316	91	0.023	6.6	4.2
C2	33	0.33	13.6	363	104	0.022	6.4	4.5
C3	10.3	0.31	8.08	87	37	0.040	7.0	1.7
C4	3	0.33	2.82	20	8.6	0.028	8.7	1.1





enough to make Coulomb blockade irrelevant. In effect, our NW devices in the 2-probe configuration mimic two similar tunnel junctions in series in the context of the FIT model.

Previously, the FIT model has been successfully applied to explain the temperature behavior of the resistances in, among others, carbon polyvinylchloride composites [71, 74, 75], polymer composites [76], and tin-doped indium oxide thin films [77]. In those “macroscopic” composite systems, a very large number of tunnel junctions with barely known junction properties were involved. On the contrary, the situation is greatly simplified and straightforward in our case, since in the 2-probe configuration we deal with only two electronic contacts characterized by similar junction parameters, as discussed. Moreover, our junction area  $A$  is known. Interestingly, our experimental values of  $w$  and  $V_0$  listed in Table 4.1 are on the same orders of magnitude to those obtained in carbon polyvinylchloride composites [71, 74, 75]. This coincidence may be due to the fact that the sizes of our NWs are approximately the same to the mean size of the conducting chains found in those composites.

Finally, it is worth noting that, if in our case, the effective junction area is somewhat reduced from the maximum possible area  $A$  defined above, our values of  $w$  ( $V_0$ ) would be slightly decreased (increased) from those listed in Table 4.1.

## 4.3 IrO<sub>2</sub>

### 4.3.1 Electron hopping conduction

In this subsection, we report the temperature behaviour of the highly resistive  $R_c(T)$  for two electronic contacts measured on a representative IrO<sub>2</sub> NW (Ir-3) connected by three submicron electrodes. The sample parameters of the Ir-3 NW are given in the caption to table 4.2. As discussed in Section 2.2, the values of  $R_c(T)$  can be extracted from the electrical measurements by employing either the 3-p [Fig. 2.5(c)] or the 2-p [Fig. 2.5(d)] configuration, provided that  $R_c \gg R_s$  and  $R_c \gg R_{el}$ . At 300 K, the resistances obtained from the 3-p and 2-p configurations for this particular NW are 2.4 and 5.6 k $\Omega$ , respectively. These

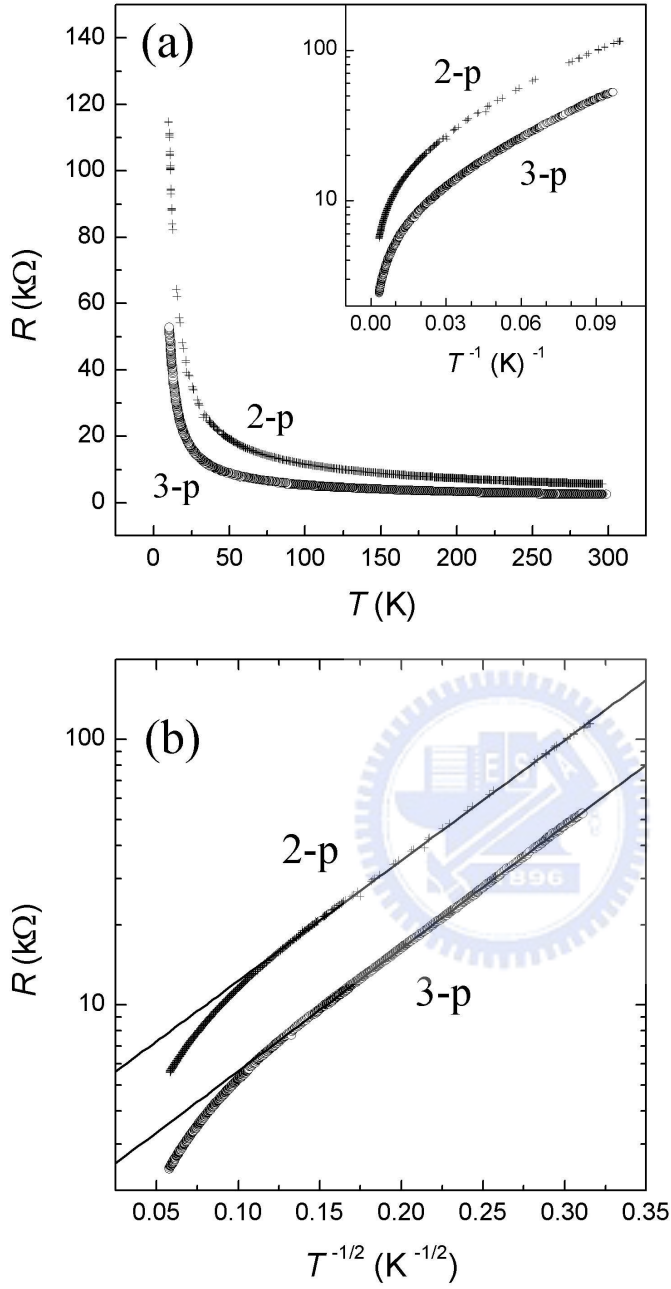
measured values are indeed significantly larger than the intrinsic resistance ( $\approx 0.5 \text{ k}\Omega$ ) of this NW, suggesting that the contact resistance(s) being dominating the measured resistances. More precisely, the measured  $R_{3-p}$  and  $R_{2-p}$  are largely determined by the electronic contact resistances  $R_{c2}$  and  $R_{c3}$  as denoted in Figs. 2.5(c) and (d). In the 3-p method, the measured resistance  $R = R_{3-p} \approx R_{c3}$ ; while in the 2-p method, the measured resistance  $R = R_{2-p} \approx R_{c2} + R_{c3}$ .

Figure 4.4(a) shows our experimental results for  $R_{3-p}$  and  $R_{2-p}$  as a function of temperature. Inspection of Fig. 4.4 indicates that, in sharp contrast to the 4-p results discussed previously, now the measured resistances also reveal semiconducting or insulating behaviour, namely, the resistance increases rapidly with decreasing temperature. Below about 50 K, a sharp resistance rise is found. Quantitatively, as the temperature reduces from room temperature to liquid-helium temperatures, the resistance ratio  $R_{2-p}/R_{4-p}$  increases from  $\approx 20$  to  $\approx 500$ , ensuring the predominance of the electronic contact resistances on the measured resistances especially at intermediate and low temperatures. The relevant parameters measured for the 3-p and 2-p configurations are listed in table 4.2.

A plot of  $\log R$  as a function of  $1/T$  is shown in the inset of Fig. 4.4(a), the nonlinear dependences of the 3-p and 2-p results suggest that the simple thermally activated conduction is not the responsible mechanism for our observations. Instead, if we plot  $\log R$  as a function of  $T^{-1/2}$ , linear dependences are clearly obeyed for a *very wide* temperature range from about 100 K down to liquid-helium temperatures, as depicted in Fig. 4.4(b). The difference between the two curves are simply the electronic contact resistance  $R_{c2}(T)$ . Such a  $\log R \propto T^{-1/2}$  behaviour is frequently observed in materials like granular metals [78] and disordered semiconductors [79]. The resistance can be expressed as

$$R(T) = R_{\infty} \exp[(T_0/T)^{1/2}] , \quad (4.4)$$

where  $R_{\infty}$  and  $T_0$  are material dependent parameters and are insensitive to temperature. Our fitted values of  $R_{\infty}$  and  $T_0$  are listed in table 4.2. In



**Figure 4.4:** (a) Resistances as a function of temperature for the 2-probe and 3-probe measurement configurations as depicted in Figs. 2.5(c) and (d). The inset shows  $\log R$  as a function of  $1/T$ . (b)  $\log R$  as a function of  $T^{-1/2}$ . Since  $R_{2-p} \approx R_{c2} + R_{c3}$  and  $R_{3-p} \approx R_{c3}$ , the difference between the two curves is simply the electronic contact resistance  $R_{c2}$ .

**Table 4.2:** Values of the relevant parameters for the three-probe and two-probe electrical measurement configurations implemented on the Ir-3 NW contacted by three submicron Cr/Au (10/90 nm) electrodes. The Ir-3 NW has a hypotenuse  $W \approx 115 \pm 5$  nm, length  $L \approx 0.7 \mu\text{m}$ , and the sample resistance  $R_s(300 \text{ K}) \approx 0.5 \text{ k}\Omega$ .  $R_\infty$  and  $T_0$  are defined in Eq. (4.4).

	$R(300 \text{ K})$ (k $\Omega$ )	$R(100 \text{ K})$ (k $\Omega$ )	$R(10 \text{ K})$ (k $\Omega$ )	$R_\infty$ (k $\Omega$ )	$T_0$ (K)
3-p	2.4	5.2	56.1	1.9	113
2-p	5.6	11.6	117.4	4.3	109



disordered semiconductors, the form of Eq. (4.4) can be given by the one-dimensional Mott [80] variable range hopping (VRH) between localized carrier states near the Fermi level, or by the Efros-Shklovskii [81] VRH if the Coulomb interaction between carriers is taken into account. In granular metals, the form of Eq. (4.4) arises from the conductivity model of Sheng and co-workers [78, 82], in which a structural effect is considered. In our case, since the 90-nm thick Au film (which formed the top layer of the submicron electrode) and the IrO<sub>2</sub> NW are “good” metals, it is conjectured that our measured resistance of  $\sim$  several tens k $\Omega$  (at a few tens K and lower) must be dominated by a resistance due to the nominally 10-nm thick *granular* Cr layer deposited *between* the thick Au film and the IrO<sub>2</sub> NW. It can also be due to the amorphous coating and/or the noncrystalline structure of the outermost one or two atomic layers of the as-grown IrO<sub>2</sub> NW. The granular structure of the deposited Cr thin layer might have accidentally formed due to the breaking induced by tensile stress, the vacancies caused by dramatic surface roughness near the contact region, or the lightly contaminated metal grains during evaporation. To check the structure, we have made several samples comprising a Cr layer with a nominal thickness of 10 nm on mica substrates using similar deposition conditions as used for the submicron electrode fabrication, and analyzed the Cr layer surface profiles by atomic force microscopy (AFM). As expected, a granular pattern with a distribution of disk-shaped grains having radius of  $\sim$  several tens nm and height of  $\approx$  2–6 nm has been observed in several cases (see Fig. 4.5), supporting the aforementioned conjecture. Indeed, it is known that thermal-evaporation deposited thin Cr films can easily form island-like granular structures rather than continuous layers [83].

Apparently, the one-dimensional Mott [80] VRH process is inappropriate for the explanation of our data, considering the geometrical structure around the contact region of our samples, namely, the size of the thin Cr layer in the transverse directions of electrical transport is more than an order of magnitude larger than that in the longitudinal direction. Although the Efros-Shklovskii [81] VRH theory is often used to fit the resistivity data in the studies of granular metals where a  $\log R \propto T^{-1/2}$  behaviour is observed, it has been shown

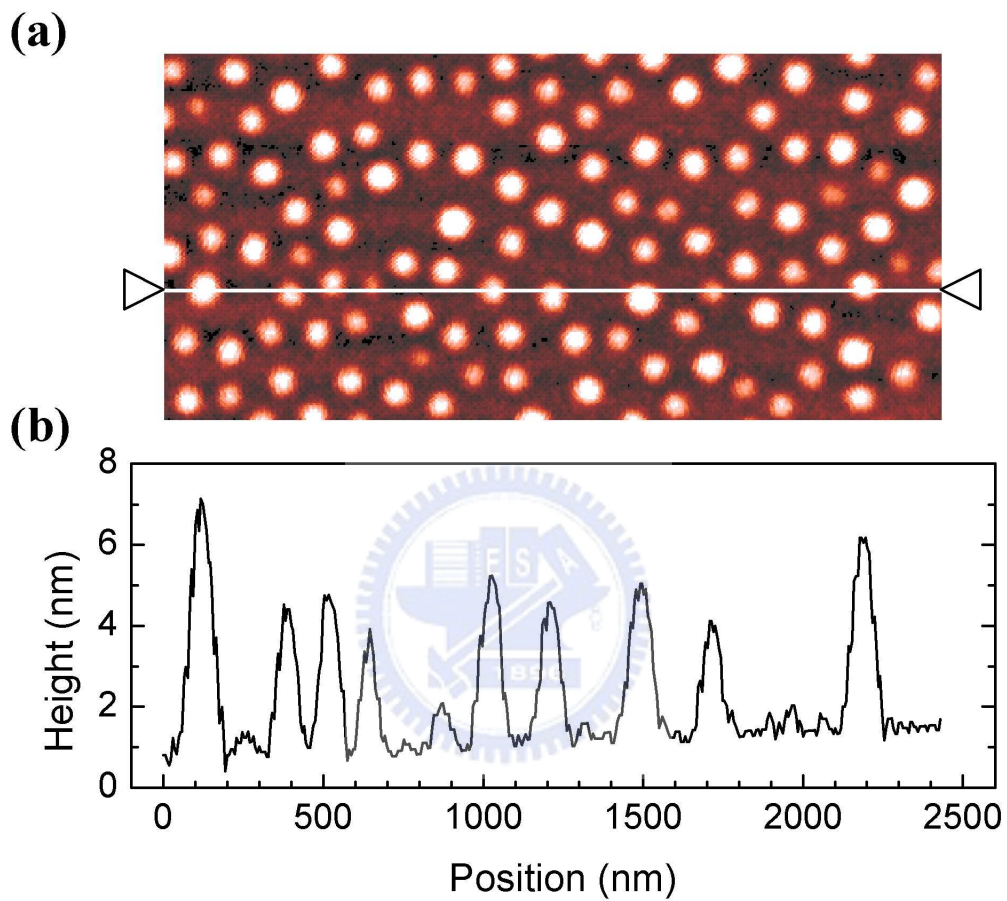


**Figure 4.5:** (a) AFM image of a thin Cr layer with a mean thickness of 10 nm prepared by thermal-evaporation deposition on a mica substrate. (b) Surface profile along the line indicated in (a), showing a distribution of disk-shaped grains having radius of  $\sim$  several tens nm and height of  $\approx 2\text{--}6$  nm.

[84, 85] that serious inconsistencies exist in applying such transport model to those systems due to the unreasonable extracted values of the relevant parameters. For instance, an optimum hop distance is found to be too short to allow the electrons to tunnel beyond neighboring metal grains, or, a tunnelling barrier is found to be smaller than  $k_B T$  (where  $k_B$  is the Boltzmann constant), and thus made the comparison unrealistic. Therefore, we believe that the adequate mechanism to describe our data is the conductivity model proposed by Sheng and co-workers [78, 82], i.e., conduction electrons are thermally activated and hop through, in our case, the nanoscale Cr granules sandwiched between the thick Au layer and the IrO<sub>2</sub> NW.

In the Sheng's model [78, 82], it is proposed that, for a granular metal-dielectric composite sample with a uniform relative volume fraction of metal and dielectric, the ratio  $s/d$  should have the same value everywhere throughout the sample, where  $s$  is the separation of neighboring metal grains, and  $d$  is the diameter of metal grains. Since the electrostatic charging energy  $E_c \sim 1/d$  (which is required to create a positive-negative charged pair of grains), it thus follows that  $sE_c$  is a constant everywhere in the sample and can be written as

$$sE_c = \frac{k_B T_0}{4\chi}, \quad (4.5)$$

where  $T_0$  is the characteristic temperature parameter in Eq. (4.4),  $\chi = (2m\phi/\hbar^2)^{1/2}$ ,  $m$  is the effective electron mass,  $\phi$  is the effective barrier height, and  $\hbar$  is Planck's constant divided by  $2\pi$ . With a second assumption that only hopping between nearest-neighbor grains which are equal or nearly equal in size is included, the model found that, at each temperature  $T$ , the maximum conductivity occurs at a dominant separation of neighboring metal grains,  $s_m$ , given by

$$s_m = \frac{1}{4\chi} \left( \frac{T_0}{T} \right)^{1/2}. \quad (4.6)$$

From Eqs. (4.5) and (4.6), it follows that, at high (low) temperatures, the conductivity is governed by the hopping events between small (large) grains separated by a short (long) distance. From our fitted value of  $T_0 \approx 110$  K, and assuming a free electron mass and a barrier height  $\phi \approx 0.1$  eV, we

obtain  $E_c \approx 16$  (3) meV and  $s_m \approx 1$  (5) Å at  $T = 300$  (10) K. (A value of  $\phi \approx 0.1$  eV corresponds to a small barrier height which is about an order of magnitude larger than the thermal energy  $k_B T$ , and is just probable for tunnelling to occur.) These values are quite close to the values obtained in the previous works on granular metallic systems [78] and suggest that our thin Cr layers lie in the dielectric regime approaching the threshold for classical percolation conductivity. The smallness of the values of  $s_m$  results from a high volume fraction of metal (Cr), which in turn renders a low value of the effective tunnelling barrier due to considerable image forces [78, 82].





## Chapter 5

### Conclusion

By using different probe configurations in our measurements, we have measured down to liquid-helium temperatures not only the intrinsic electronic transport properties of individual single-crystalline RuO<sub>2</sub> and IrO<sub>2</sub> NWs but also the temperature dependent behaviours of high-resistance electronic contacts  $R_c$  on these two kinds of NWs.

For the intrinsic properties of the NWs, although the measured temperature dependent resistivities can be well accounted for by an existing theoretical description based on the Boltzmann transport theory, we found that the Debye temperature in RuO<sub>2</sub> NWs is largely reduced as the diameter of the NW decreases. (Comparable experiments on IrO<sub>2</sub> NWs with diameters down to this scale have not been performed.) Possible mechanisms accounting for this observation have been discussed. It is concluded that the chemical binding in the NWs may be gradually weakened as the diameter decreases.

By employing the 3- and 2-probe method, we have quantitatively characterized the temperature behaviours of high resistance electronic contacts,  $R_c$ , formed at the interfaces between the submicron electrodes and the NWs. Two different behaviours have been observed. For RuO<sub>2</sub> NWs, we found that the temperature dependence of the  $R_c$  can be well attributed to the thermally fluctuation-induced tunneling conduction through a junction formed at the interface between the electrode and the NW. The junction parameters such as the barrier width and height have been determined. On the other hand, For IrO<sub>2</sub> NWs, a temperature behaviour obeying the law  $\log R \propto T^{-1/2}$  is observed over a wide temperature range below  $\approx 100$  K. This behaviour is satisfactorily ascribed to the hopping of electrons through nanoscale Cr granules and/or amorphous coating incidentally formed at the interface between the Cr/Au submicron electrode and the NW. Less direct evidence supporting

this argument has been provided.

This work demonstrates that, by properly applying a combination of electrical measurement configurations, both the intrinsic property of a NW and the electronic contact on it could be quantitatively studied. Under certain conditions, the electronic contacts between an interconnect and a metal nanodevice could be further modeled.



## References

- [1] S. Frank, P. Poncharal, Z. L. Wang, and W. A. de Heer, *Science* **280**, 1744 (1998).
- [2] S. J. Tans, A. R. M. Verschueren, and C. Dekker, *Nature* **393**, 49 (1998).
- [3] J. G. Lu, P. Chang, and Z. Fan, *Mater. Sci. Eng. R* **52**, 49 (2006).
- [4] Y. Cui and C. M. Lieber, *Science* **291**, 851 (2001).
- [5] H. Kind, H. Yan, B. Messer, M. Law, and P. Yang, *Adv. Mater.* **14**, 158 (2002).
- [6] Y. Huang, X. Duan, Y. Cui, and C. M. Lieber, *Nano Lett.* **2**, 101 (2002).
- [7] Y. Wu, J. Xiang, C. Yang, W. Lu, and C. M. Lieber, *Nature* **430**, 61 (2004).
- [8] S. B. Cronin, Y. M. Lin, O. Rabin, M. R. Black, J. Y. Ying, M. S. Dresselhaus, P. L. Gai, J. P. Minet, and J. P. Issi, *Nanotechnology* **13**, 653 (2002).
- [9] A. Boukai, K. Xu, and J. R. Heath, *Adv. Mater.* **18**, 864 (2006).
- [10] J. V. Ryan, A. D. Berry, M. L. Anderson, J. W. Long, R. M. Stroud, V. M. Cepak, V. M. Browning, D. R. Rolison, and C. I. Merzbacher, *Nature* **406**, 169 (2000).
- [11] C. C. Chen, R. S. Chen, T. Y. Tsai, Y. S. Huang, D. S. Tsai, and K. K. Tiong, *J. Phys.: Condens. Matter* **16**, 8475 (2004).
- [12] Y. T. Lin, C. Y. Chen, C. P. Hsiung, K. W. Cheng, and J. Y. Gan, *Appl. Phys. Lett.* **89**, 063123 (2006).
- [13] B. C. Satishkumar, A. Govindaraj, M. Nath, and C. N. R. Rao, *J. Mater. Chem.* **10**, 2115 (2000).
- [14] C. Ducati, D. H. Dawson, J. R. Saffell, and P. A. Midgley, *Appl. Phys. Lett.* **85**, 5385 (2004).

- [15] Y. L. Liu, Z. Y. Wu, K. J. Lin, J. J. Huang, F. R. Chen, J. J. Kai, Y. H. Lin, W. B. Jian, and J. J. Lin, *Appl. Phys. Lett.* **90**, 013105 (2007).
- [16] K. Ip, Y. W. Heo, K. H. Baik, D. P. Norton, S. J. Pearton, S. Kim, J. R. LaRoche, and F. Ren, *Appl. Phys. Lett.* **84**, 2835 (2004).
- [17] G. Gu, M. Burghard, G. T. Kim, G. S. Düsberg, P. W. Chiu, V. Krstic, S. Roth, and W. Q. Han, *J. Appl. Phys.* **90**, 5747 (2001).
- [18] W. D. Ryden, A. W. Lawson, and C. C. Sartain, *Phys. Rev. B* **1**, 1494 (1970).
- [19] J. J. Lin, S. M. Huang, Y. H. Lin, T. C. Lee, H. Liu, X. X. Zhang, R. S. Chen, and Y. S. Huang, *J. Phys.: Condens. Matter* **16**, 8035 (2004).
- [20] S. Trasatti and G. Lodi, in *Electrodes of Conductive Metallic Oxides, Part B*, edited by S. Trasatti chap. 10 Elsevier 1981.
- [21] S. Trasatti, *Electrochim. Acta* **36**, 225 (1991).
- [22] G. K. White and P. J. Meeson, *Experimental Techniques in Low-Temperature Physics*, 4 ed. (Oxford University Press, 2002).
- [23] A. T. Kuhn and C. J. Mortimer, *J. Electrochem. Soc.* **120**, 231 (1973).
- [24] B. E. Conway, V. Birss, and J. Wojtowicz, *J. Power Sources* **66**, 1 (1997).
- [25] M. W. Shafer and J. Armstrong, *IBM Tech. Disc. Bull.* **20**, 4633 (1978).
- [26] D. J. Pedder, *Electrocompon. Sci. Technol.* **2**, 259 (1976).
- [27] E. Kolawa, F. C. T. So, E. T.-S. Pan, and M.-A. Nicolet, *Appl. Phys. Lett.* **50**, 854 (1987).
- [28] R. S. Wagner and W. C. Ellis, *Appl. Phys. Lett.* **4**, 89 (1964).
- [29] C. U. Pinnow, I. Kasko, C. Dehm, B. Jobst, M. Seibt, and U. Geyer, *J. Vac. Sci. Technol. B* **19**, 1857 (2001).
- [30] S. F. Cogan, T. D. Plante, R. S. McFadden, and R. D. Rauh, *Sol. Energy Mater.* **16**, 371 (1987).
- [31] T. Nakamura, Y. Nakao, A. Kamisawa, and H. Takasu, *Appl. Phys. Lett.* **65**, 1522 (1994).

- [32] A. Osaka, T. Takatsuna, and Y. Miura, *J. Non-Cryst. Solids* **178**, 313 (1994).
- [33] R. S. Chen, Y. S. Huang, Y. M. Liang, C. S. Hsieh, D. S. Tsai, and K. K. Tiong, *Appl. Phys. Lett.* **84**, 1552 (2004).
- [34] R. S. Chen, H. M. Chang, Y. S. Huang, D. S. Tsai, and K. C. Chiu, *Nanotechnology* **16**, 93 (2005).
- [35] R. S. Chen, H. M. Chang, Y. S. Huang, D. S. Tsai, S. Chattopadhyay, and K. H. Chen, *J. Cryst. Growth* **271**, 105 (2004).
- [36] Keithley Instruments, *Low Level Measurements Handbook*, 6 ed. (Keithley Instruments, 2004).
- [37] J. E. Graebner, E. S. Greiner, and W. D. Ryden, *Phys. Rev. B* **13**, 2426 (1976).
- [38] G. K. Wertheim and H. J. Guggenheim, *Phys. Rev. B* **22**, 4680 (1980).
- [39] E. H. P. Cordfunke, R. J. M. Konings, E. F. Westrum, Jr., and R. Shaviv, *J. Phys. Chem. Solids* **50**, 429 (1989).
- [40] A. K. Goel, G. Skorinko, and F. H. Pollak, *Phys. Rev. B* **24**, 7342 (1981).
- [41] L. F. Mattheiss, *Phys. Rev. B* **13**, 2433 (1976).
- [42] K. M. Glassford and J. R. Chelikowsky, *Phys. Rev. B* **47**, 1732 (1993).
- [43] K. M. Glassford and J. R. Chelikowsky, *Phys. Rev. B* **49**, 7107 (1994).
- [44] J. H. Xu, T. Jarlborg, and A. J. Freeman, *Phys. Rev. B* **40**, 7939 (1989).
- [45] J. S. de Almeida and R. Ahuja, *Phys. Rev. B* **73**, 165102 (2006).
- [46] C. Y. Wu, H. Y. Jian, S. M. Mar, Y. S. Huang, and J. J. Lin, *Chin. J. Phys.* **34**, 784 (1996).
- [47] J. J. Lin, W. Xu, Y. L. Zhong, J. H. Huang, and Y. S. Huang, *Phys. Rev. B* **59**, 344 (1999).
- [48] S. S. Yeh, J. J. Lin, X. N. Jing, and D. L. Zhang, *Phys. Rev. B* **72**, 024204 (2005).
- [49] J. S. Dugdale, *The Electrical Properties of Metals and Alloys* (Edward Arnold, London, 1977).

- [50] D. B. Poker and C. E. Klabunde, *Phys. Rev. B* **26**, 7012 (1982).
- [51] P. A. Lee and T. V. Ramakrishnan, *Rev. Mod. Phys.* **57**, 287 (1985).
- [52] R. W. Cochrane, R. Harris, J. O. Ström-Olson, and M. J. Zuckermann, *Phys. Rev. Lett.* **35**, 676 (1975).
- [53] P. M. T. M. van Attekum, P. H. Woerlee, G. C. Verkade, and A. A. M. Hoeben, *Phys. Rev. B* **29**, 645 (1984).
- [54] Y. P. Lee, Y. V. Kudryavtsev, V. V. Nemoshkalenko, J. Y. Rhee, and K. W. Kim, *J. Appl. Phys.* **91**, 4364 (2002).
- [55] C. Ettl and K. Samwer, *J. Non-Cryst. Solids* **156–158**, 502 (1993).
- [56] J. Cieslak, B. F. O. Costa, S. M. Dubiel, M. Reissner, and W. Steiner, *J. Phys.: Condens. Matter* **16**, L343 (2004).
- [57] M. X. Gu, C. Q. Sun, Z. Chen, T. C. A. Yeung, S. Li, C. M. Tan, and V. Nosik, *Phys. Rev. B* **75**, 125403 (2007).
- [58] P. R. Couchman and F. E. Karasz, *Phys. Lett.* **62A**, 59 (1977).
- [59] M. Yu. Reizer and A. V. Sergeev, *Zh. Eksp. Teor. Fiz.* **92**, 2291 (1987) [*Sov. Phys. JETP* **65**, 1291 (1987)].
- [60] N. G. Ptitsina, G. M. Chulkova, K. S. Il'in, A. V. Sergeev, F. S. Pochinkov, E. M. Gershenson, and M. E. Gershenson, *Phys. Rev. B* **56**, 10089 (1997).
- [61] P. M. Echternach, M. E. Gershenson, and H. M. Bozler, *Phys. Rev. B* **47**, 13659 (1993).
- [62] S. Kim, H. Suhl, and I. K. Schuller, *Phys. Rev. Lett.* **78**, 322 (1997).
- [63] A. A. Balandin, *J. Nanosci. Nanotech.* **5**, 1 (2005).
- [64] M. V. Klein, *IEEE J. Quantum Electron.* **22**, 1986 (1986).
- [65] N. Nishiguchi, Y. Ando, and M. N. Wybourne, *J. Phys.: Condens. Matter* **9**, 5751 (1997).
- [66] N. A. Bannov, V. V. Mitin, and M. A. Stroscio, in *Quantum Transport in Ultrasmall Devices*, edited by D. K. F. et al. p. 191 Plenum Press, New York 1995.

- [67] C. Kittel, *Introduction to Solid State Physics* (John Wiley & Sons, 2005).
- [68] C. Q. Sun, L. K. Pan, C. M. Li, and S. Li, *Phys. Rev. B* **72**, 134301 (2005).
- [69] A. Bid, A. Bora, and A. K. Raychaudhuri, *Phys. Rev. B* **74**, 035426 (2006).
- [70] A. Buldum and J. P. Lu, *Phys. Rev. B* **63**, 161403 (2001).
- [71] P. Sheng, E. K. Sichel, and J. I. Gittleman, *Phys. Rev. Lett.* **40**, 1197 (1978).
- [72] P. Sheng, *Phys. Rev. B* **21**, 2180 (1980).
- [73] M. Tinkham, D. Davidović, D. C. Ralph, and C. T. Black, *J. Low Temp. Phys.* **118**, 271 (2000).
- [74] E. K. Sichel, J. I. Gittleman, and P. Sheng, *Phys. Rev. B* **18**, 5712 (1978).
- [75] E. K. Sichel, P. Sheng, J. I. Gittleman, and S. Bozowski, *Phys. Rev. B* **24**, 6131 (1981).
- [76] S. Paschen, M. N. Bussac, L. Zuppiroli, E. Minder, and B. Hilti, *J. Appl. Phys.* **78**, 3230 (1995).
- [77] J. Ederth, P. Johnsson, G. A. Niklasson, A. Hoel, A. Hultåker, P. Heszler, C. G. Granqvist, A. R. van Doorn, M. J. Jongerius, and D. Burgard, *Phys. Rev. B* **68**, 155410 (2003).
- [78] B. Abeles, P. Sheng, M. D. Coutts, and Y. Arie, *Adv. Phys.* **24**, 407 (1975).
- [79] D. Redfield, *Adv. Phys.* **24**, 463 (1975).
- [80] N. F. Mott and E. A. Davis, *Electronic Processes in Non-Crystalline Materials* (Oxford University Press, 1979).
- [81] B. I. Shklovskii and A. L. Efros, *Electronic Properties of Doped Semiconductors* (Springer, 1984).
- [82] P. Sheng, B. Abeles, and Y. Arie, *Phys. Rev. Lett.* **31**, 44 (1973).
- [83] P. A. Gould, *Brit. J. Appl. Phys.* **16**, 1481 (1965).

- [84] C. J. Adkins, *J. Phys.: Condens. Matter* **1**, 1253 (1989).
- [85] C. J. Adkins, in *Hopping and Related Phenomena*, edited by H. Fritzsche and M. Pollak p. 93 World Scientific 1990.

